An improved splitting algorithm for unsteady generalized Newtonian fluid flow problems with natural boundary conditions

Anouar Obbadi[1], Mofdi El-Amrani[1], Mohammed Seaid[2,*], Driss Yakoubi[3]

[1] *Laboratory of Mathematics and Applications, FSTT, Abdelmalek Essaadi University, Tangier, Morocco.*
Email: anouar.obbadi@etu.uae.ac.ma, mofdi.elamrani@gmail.com
[2] *Department of Engineering, University of Durham, South Road, Durham DH1 3LE, United Kingdom.*
Email: m.seaid@durham.ac.uk
[3] *Léonard de Vinci Pôle Universitaire, Research Center, 92 916 Paris La Défense, France.*
Email: driss.yakoubi@devinci.fr

Abstract

Generalized Newtonian fluids are challenging to solve using the standard projection or fractional-step methods which split the diffusion term from the incompressibility constraint during the time integration process. Most of this class numerical methods already suffer from some inconsistencies, even in the Newtonian case, due to unphysical pressure boundary conditions which deteriorate the quality of approximations especially when open boundary conditions are prescribed in the problem under study. The present study proposes an improved viscosity-splitting approach for solving the generalized Newtonian fluids in which the viscosity follows a nonlinear generic rheological law. This method consists of decoupling the convective effects from the incompressibility while keeping a diffusion term in the last step allowing to enforce consistent boundary conditions. We provide a full algorithmic description of the method accounting for both Dirichlet and Neumann boundary conditions. To evaluate the computational performance of the proposed viscosity-splitting algorithm, we present numerical results for an example with manufactured exact solution and for the benchmark problems of lid-driven cavity flow and flow past a circular cylinder. We also assess the accuracy of the method for an unsteady flow around an arrangement of two cylinders in tandem and comparisons with results obtained using a monolithic approach reveal good general agreement.

Keywords. Non-Newtonian fluids; Navier-Stokes equations; Viscosity-splitting algorithm; Finite element method.

1 Introduction

The fluid behavior in a flow problem is closely linked to the viscous properties of the fluid itself which vary from one fluid to another based on the relation between the shear stress and the shear rate. A fluid where the shear stress depends linearly on the shear rate is considered as Newtonian while, non-Newtonian fluids are characterized by a nonlinear dependency between the shear stress and the deformation rate. In addition, generalized Newtonian fluids are a special subclass incubating the non-Newtonian fluids that preserves the tensorial structure of the Newtonian model. In other words, the nonlinearity in the shear stress, as a function of the shear rate, is contained in the viscosity which becomes in this case, an explicit nonlinear function of the shear stress. Thus, the viscosity response towards the deformation rate felt by the fluid is the dividing line between shear-thinning and shear-thickening fluids. Here, the shear-thinning (or pseudo-plastic) fluids manifest a decreasing viscosity when subjected to an increasing shear rate, and are the vast majority of real non-Newtonian fluids such as biological fluids, mayonnaise, ketchup, and most of polymer melts among others. On the other hand, the shear-thickening fluids exhibit the opposite behavior and are less encountered

*Corresponding author

in real-life applications. Several rheological models have been proposed in order to represent the generalized Newtonian fluids features including the power-law, Carreau, Carreau-Yasuda, Cross, Casson and other models, see for instance [37, 35]. There is an increasing focus among researchers on understanding the behavior of non-Newtonian fluids in a wide range of flow configurations and domains due to the growing involvement of these fluids in many biological and industrial processes in polymers, chemical engineering, slurry transport, blood flow in arteries among others. However, due to the nonlinearity introduced by the shear stress-shear rate law, the resulting equations governing the flow are even more challenging than the Newtonian case both theoretically and numerically.

It is well known that the difficulty of approximating the incompressible Navier-Stokes equations arise from the velocity-pressure coupling (in a saddle point structure) which yields poorly conditioned systems to solve. To tackle this issue, a vast family of fractional-step methods (or splitting operators) have been proposed in the literature. This category of methods, generally, tend to separate the velocity and the pressure solutions by splitting the time-marching into several (mostly two or three) substeps. It was initiated by the works of Chorin [11] and Temam [54] on the well-established projection methods. In the original version of projection methods [54], the incompressibility is separated from the convection-diffusion terms by the introduction of an intermediate velocity in the first step, that will be projected on a solenoidal space in the second step, to enforce the incompressibility. However, the boundary conditions imposed in the projection step are incompatible with the original problem, which creates an artificial (nonphysical) Neumann boundary condition on the pressure solution leading to the creation of a numerical boundary layer and a degradation of convergence rate in the $\mathbf{H}^1$-norm even with higher-order time-stepping schemes [55, 32]. Authors in [28] suggested a first-order pressure extrapolation in the first step yielding the so-called incremental pressure correction method which although has succeeded to somehow improve the $\mathbf{H}^1$-convergence of the velocity and the L^2-convergence of the pressure, it still suffers from an inconsistent Neumann boundary condition on the pressure. A rotational version of the incremental projection method has also been proposed in [56] which offered a more consistent boundary condition on the pressure and improved the convergence rate when using a second-order difference formula as in [33]. However, this method is only available for Newtonian flows as it assumes a constant viscosity in its implementation. Another way to overcome the drawback related to numerical boundary layers was introduced in [5] and it consisted of including a viscous term in the projection step and imposing the original boundary conditions on the end-of-step velocity, which ensures its convergence along with the intermediate velocity in both $\mathbf{L}^2$ and $\mathbf{H}^1$ norms. This approach, consisting of not fully uncouple the diffusion from the incompressibility allowing to preserve the true boundary conditions on the velocity, was also proposed in other methods in the literature, see for example [27, 43, 45], but for Newtonian flows only.

As far as projection methods are concerned, despite being extensively studied and analyzed in the framework of Newtonian flows, little advances can be found in the non-Newtonian case. In [23] a method has been proposed to decouple the fully discrete pressure and velocity of a power-law viscoelastic fluid using the fractional-step approach introduced in [16] which is a two-step projection based on a generalized block LU decomposition of the original saddle-point matrix of the fully discretized problem. A hybrid FVM/FEM combined with an incremental pressure correction scheme was proposed in [24] for power-law fluids. In [36] the performance of a semi-implicit Chorin projection is compared with the LBM and Runge-Kutta schemes on both shear-thinning and shear-thickening power-law fluids in the context of sudden expansion flows. A non-incremental pressure-correction method was also employed in [38] to solve power-law fluid flows in a three-dimensional lid-driven cavity for different Reynolds numbers. In [2], a non-incremental pressure correction scheme was applied but combined with an explicit Adams-Bashforth method for the convective and diffusive terms solving a class of Oldroyd-B viscoelastic fluids interacting with an elastic structure. Other approaches, not based on projection methods, have also been studied in the literature including for example [22] where the three-field formulation of an Oldroyd-B fluid is discretized in time with explicit treatment of the convective terms using a splitting operator from [44], and the fully discrete system, reformulated into an Uzawa system form, is solved with conjugate gradient method equipped with a robust preconditioner. Techniques based on least-square finite elements for stationary viscoelastic flows can also be found for example in [40, 15, 41, 20, 9, 10, 30]. Recently, authors in [17] developed, based on appropriate modifications in the incremental projection method, an efficient method known as Shear Rate Projection (SRP) suitable for flows with heterogeneous viscosity. Compared to

the conventional projection methods, the SRP method results in a more consistent pressure approximation with an improved accuracy. In [18], authors further developed the SRP approach to suit the generalized Newtonian fluids and take advantage of the dependency between the viscosity and the shear-rate stress. In [50] the same approach previously proposed in [17] was modified by introducing new pressure corrections that account for natural boundary conditions and the obtained method was shown to retrieve the advantages of the rotational projection scheme even with heterogeneous viscosity. In addition, another efficient splitting method was developed in [48] based on the technique studied in [42] that replaces the incompressibility constraint with a Poisson equation for the pressure equipped with consistent boundary conditions and results in decoupling the computation of the velocity and the pressure. Apparently, to our knowledge, the approximation of generalized Newtonian flows with viscosity-splitting methods is still inexistent.

In the present study we propose, based on the fractional-step procedure introduced in [5], a viscosity-splitting method which is suitable for generalized Newtonian flows. The proposed method belongs to a class of two-step splitting schemes for which the first step computes an intermediate velocity by solving a linear problem without accounting for both the incompressibility constraint and the pressure variable. In this first step, the convective term is linearized in a Newton-like fashion and the viscosity function that depends on the shear-rate tensor is treated explicitly to make the nonlinearity disappear. In the second step, the pressure and the incompressibility are fully recovered along with the presence of a viscous correction term which yields a Stokes problem on one hand, and on the other hand, allows to prescribe the full original boundary conditions on the end-of-step velocity. We also implement in this work an improved version of the proposed viscosity-splitting scheme using a pressure correction procedure. To verify this approach, numerical results for a three-dimensional example with known exact solution and for the two-dimensional benchmark problems of lid-driven cavity flow and flow past a circular cylinder are presented. We also perform elaborated comparisons, in terms of accuracy and efficiency, between the proposed method and the conventional viscosity-splitting method traditionally used in the literature for incompressible Navier–Stokes equations. Our findings inform applied scientists to consider the accelerated viscosity-splitting method as a practical alternative numerical algorithm for solving flow problems of generalized Newtonian fluids.

The rest of this paper is structured as follows: the viscosity-splitting methods for unsteady generalized Newtonian fluid flows is presented in Section 2. This section includes the governing mathematical equations, notations along with the time integration procedures. The finite element method for spatial discretization is formulated in Section 3. In this section we also present the algorithmic implementation of the improved viscosity-splitting algorithm for the unsteady generalized Newtonian fluid flow problems. Numerical results obtained for three test examples of non-Newtonian fluid flows are analyzed in Section 4. Conclusions are summarized in Section 5.

2 Viscosity-splitting methods for generalized Newtonian fluid flows

Let Ω be a smooth domain in $\mathbb{R}^d$ (with $d = 2$ or 3) satisfying the well-established inf–sup conditions as those discussed in [26] and let $[0, T]$ be the time interval with $T > 0$ is the final time. The boundary of Ω is splitted in two parts as $\partial\Omega = \Gamma_D \cup \Gamma_N$ with $\Gamma_D \cap \Gamma_N = \emptyset$ (possibly $\Gamma_N = \emptyset$). We also introduce the notation $\Omega_t = [0, T] \times \Omega$ for the space-time domain and $\boldsymbol{n}$ denotes the unit outward normal vector to the boundary $\partial\Omega$. In the present study, we consider unsteady flow problems of generalized Newtonian fluids *i.e.*, fluids having a non-homogeneous viscosity ν depending on time t, space $\boldsymbol{x}$, velocity $\boldsymbol{u}(t, \boldsymbol{x})$ or shear rate of the fluid $\mathbf{D}\boldsymbol{u}$, the pressure $p(t, \boldsymbol{x})$ and/or other external quantities and following a constitutive relation as

$$\sigma(\boldsymbol{u}, p) = -p\mathbf{I} + 2\nu\mathbf{D}\boldsymbol{u},$$

where $\mathbf{I}$ is the unit matrix and the shear rate $\mathbf{D}\boldsymbol{u}$ is defined by

$$\mathbf{D}\boldsymbol{u} = \frac{1}{2}\left(\nabla\boldsymbol{u} + \nabla\boldsymbol{u}^\top\right).$$

Assuming incompressible flows, the governing equations for the velocity $\boldsymbol{u}$ and pressure p can be well described by the Navier-Stokes equations as

$$\begin{aligned} \frac{\partial \boldsymbol{u}}{\partial t} + (\boldsymbol{u}\cdot\nabla)\,\boldsymbol{u} - \nabla\cdot(2\nu\mathbf{D}\boldsymbol{u}) + \nabla p &= \boldsymbol{f}, \qquad \text{in} \quad \Omega_t, \\ \nabla\cdot\boldsymbol{u} &= 0, \qquad \text{in} \quad \Omega_t, \end{aligned} \tag{1}$$

where $\boldsymbol{f}(t,\boldsymbol{x})$ represents an external volumic force such as gravity. For the viscosity ν, there exists various rheological laws widely used in industrial applications to model a shear rate dependent viscosity. Here, all the following generic laws are covered

$$\nu(\mathbf{D}\boldsymbol{u}) = \begin{cases} C\|\mathbf{D}\boldsymbol{u}\|^{m-1}, & \text{(power-law)} \quad (2) \\ \nu_\infty + (\nu_0-\nu_\infty)\left(C_0+\lambda^2\|\mathbf{D}\boldsymbol{u}\|^2\right)^{\frac{m-1}{2}}, & \text{(Carreau)} \quad (3) \\ \left(\sqrt{\mu}+\sqrt{\dfrac{\tau}{\|\mathbf{D}\boldsymbol{u}\|}}\right)^2, & \text{(Casson)} \quad (4) \\ \nu_\infty + (\nu_0-\nu_\infty)\left(1+\lambda^a\|\mathbf{D}\boldsymbol{u}\|^a\right)^{\frac{m-1}{a}}, & \text{(Carreau-Yasuda)} \quad (5) \end{cases}$$

where C is a consistency parameter of the power-law relation (2) and it has the unit Pas^m, m, C_0, μ, λ, a, ν_∞ and ν_0 are nonnegative constants to be selected for each type of fluid, τ is the shear stress assumed to be less than the maximum shear stress τ_{max}, see for example [37] for more details on these laws. In (2)-(5), $\|\cdot\|$ denotes the Euclidean norm in $\mathbb{R}^{d\times d}$. Note that the constitutive relations (2)-(5) covers a wide range of rheological models used in various flow problems and by setting $m=1$ in (2),(3) or (5), one recovers the conventional Navier-Stokes equations for a Newtonian fluid with constant viscosity. The equations for shear-thinning and shear-thickening are obtained when $m<1$ and $m>1$, respectively. It should be noted that the above laws (2)-(5) suffer from a typical numerical challenge as the associated viscosity could reach nonphysical values such as zero or infinite viscosity. This can be overcome following ideas reported in [51] among others, by setting upper and lower thresholds beyond which the viscosity is frozen. Notice that for the flow problems of generalized Newtonian fluids considered in this study, this cut-off has not been used in the simulations.

On the domain boundary $\partial\Omega$, we consider non-homogeneous Dirichlet boundary conditions on Γ_D as

$$\boldsymbol{u} = \boldsymbol{g}_D, \qquad \text{on} \quad [0,T]\times\Gamma_D, \tag{6}$$

and Neumann boundary condition on Γ_N as

$$\sigma(\boldsymbol{u},p)\cdot\boldsymbol{n} = \boldsymbol{g}_N, \qquad \text{on} \quad [0,T]\times\Gamma_N, \tag{7}$$

where $\boldsymbol{g}_D(t,\boldsymbol{x})$ and $\boldsymbol{g}_N(t,\boldsymbol{x},)$ are given boundary functions. At time $t=0$,

$$\boldsymbol{u}(0,\boldsymbol{x}) = \boldsymbol{u}_0(\boldsymbol{x}), \qquad \text{in} \quad \Omega, \tag{8}$$

where $\boldsymbol{u}_0(\boldsymbol{x})$ is a given initial function. It should be stressed that the existence and regularity of the solution for the case of Newtonian fluids ($m=1$) has been studied in [4, 53, 21] among others. In the case of non-Newtonian fluids ($m\neq 1$), existence of a solution of the problem (1)-(8) has been proved under some assumptions on the viscosity ν, see for example [21, 3, 19].

To solve the boundary-value problem defined by (1)-(8), we first divide the time interval $[0,T]$ into N subintervals $[t_n,t_{n+1}]$ with a time step $\Delta t = t_{n+1}-t_n$ for $n=0,1,\ldots,N$. We use the notations $\boldsymbol{f}^n=\boldsymbol{f}(t_n,\boldsymbol{x})$, $\boldsymbol{g}_D^n=\boldsymbol{g}_D(t_n,\boldsymbol{x})$, $\boldsymbol{g}_N^n=\boldsymbol{g}_N(t_n,\boldsymbol{x})$, and we denote by $\boldsymbol{u}^n$ and p^n the approximations at time t_n of the solution $\boldsymbol{u}$ and p, respectively. Hence, Applied to equations (1)-(8), the conventional Viscosity-Splitting (VS) method is carried out using the following two steps:

Step 1: Given $\boldsymbol{u}^n$ at time t_n, compute the intermediate velocity $\widetilde{\boldsymbol{u}}^{n+1}$ as

$$\begin{aligned}
\frac{\widetilde{\boldsymbol{u}}^{n+1}-\boldsymbol{u}^n}{\Delta t}+\widetilde{\boldsymbol{u}}^{\star,n+1}\cdot\nabla\widetilde{\boldsymbol{u}}^{n+1}-\nabla\cdot\left(2\nu\left(\boldsymbol{D}\boldsymbol{u}^n\right)\boldsymbol{D}\widetilde{\boldsymbol{u}}^{n+1}\right) &= \boldsymbol{f}^{n+1}, && \text{in} \quad \Omega,\\
\widetilde{\boldsymbol{u}}^{n+1} &= \boldsymbol{g}_D^{n+1}, && \text{on} \quad \Gamma_D,\\
\nu(\boldsymbol{D}\boldsymbol{u}^n)\boldsymbol{D}\widetilde{\boldsymbol{u}}^{n+1}\cdot\boldsymbol{n} &= p^n\boldsymbol{n}+\boldsymbol{g}_N^{n+1}, && \text{on} \quad \Gamma_N.
\end{aligned} \tag{9}$$

Step 2: Given $\widetilde{\boldsymbol{u}}^{n+1}$ from **Step 1**, compute the solution $\left(\boldsymbol{u}^{n+1},p^{n+1}\right)$ of the Stokes problem as

$$\begin{aligned}
\frac{\boldsymbol{u}^{n+1}-\widetilde{\boldsymbol{u}}^{n+1}}{\Delta t}-\nabla\cdot\left(2\nu\left(\boldsymbol{D}\boldsymbol{u}^n\right)\left(\boldsymbol{D}\boldsymbol{u}^{n+1}-\boldsymbol{D}\widetilde{\boldsymbol{u}}^{n+1}\right)\right)+\nabla p^{n+1} &= 0, && \text{in} \quad \Omega,\\
\nabla\cdot\boldsymbol{u}^{n+1} &= 0, && \text{in} \quad \Omega,\\
\boldsymbol{u}^{n+1} &= \boldsymbol{g}_D^{n+1}, && \text{on} \quad \Gamma_D,\\
\left(-p^{n+1}\boldsymbol{I}+2\nu\left(\boldsymbol{D}\boldsymbol{u}^n\right)\boldsymbol{D}\boldsymbol{u}^{n+1}\right)\cdot\boldsymbol{n} &= \boldsymbol{g}_N^{n+1}, && \text{on} \quad \Gamma_N.
\end{aligned} \tag{10}$$

Note that the two sources of nonlinearities in the above VS method namely, the convective term and the viscous term, are linearized as follow:

(i) The nonlinearity originated from the viscous term in (9)-(10) is treated explicitly by taking $\nu\left(\boldsymbol{D}\boldsymbol{u}^n\right)$ instead of $\nu(\mathbf{D}\widetilde{\boldsymbol{u}}^{n+1})$. However, this choice would need additional processing using a fixed-point like solver.

(ii) The convective term in (9) can be linearized by taking $\widetilde{\boldsymbol{u}}^{\star,n+1}=\boldsymbol{u}^n$, but a better choice consists of adopting a Newton-like approach which produces additional terms. In this case, the first equation in (9) is replaced by

$$\frac{\widetilde{\boldsymbol{u}}^{n+1}-\boldsymbol{u}^n}{\Delta t}+\boldsymbol{u}^n\cdot\nabla\widetilde{\boldsymbol{u}}^{n+1}+\widetilde{\boldsymbol{u}}^{n+1}\cdot\nabla\boldsymbol{u}^n-\nabla\cdot\left(2\nu\left(\boldsymbol{D}\boldsymbol{u}^n\right)\mathbf{D}\widetilde{\boldsymbol{u}}^{n+1}\right)=\boldsymbol{f}^{n+1}+\boldsymbol{u}^n\cdot\nabla\boldsymbol{u}^n. \tag{11}$$

It should be stressed that in Step 2, viscous terms are still present alongside with the original boundary conditions on the end-of-step velocity $\boldsymbol{u}^{n+1}$. Those terms are the major differences between the viscosity-splitting method and the standard projection methods, see for instance [34]. However, thanks to this feature of the VS method, one does not have to bother about any inconsistent boundary conditions for the pressure solution. Notice that, it is also possible to replace the viscous term $\nu\left(\boldsymbol{D}\boldsymbol{u}^n\right)$ in (10) by $\nu(\mathbf{D}\widetilde{\boldsymbol{u}}^{n+1})$ or by $\theta\nu\left(\boldsymbol{D}\boldsymbol{u}^n\right)+(1-\theta)\nu(\mathbf{D}\widetilde{\boldsymbol{u}}^{n+1})$ with $\theta\in[0,1]$ without loosing the linear structure of the problem.

In the present work, we modify the conventional viscosity-splitting method by adopting a pressure-correction procedure [28, 57]. Thus, instead of neglecting the pressure, we add an old pressure term ∇p^n to the first step, and then update the actual pressure in the second step. The resulting Improved Viscosity-Splitting (IVS) method considered in this study to solve the equations (1)-(8) is carried out using the following two steps:

Step 1: Given $\boldsymbol{u}^n$ at time t_n, compute the intermediate velocity $\widetilde{\boldsymbol{u}}^{n+1}$ as

$$\begin{aligned}
\frac{\widetilde{\boldsymbol{u}}^{n+1}-\boldsymbol{u}^n}{\Delta t}+\boldsymbol{u}^n\cdot\nabla\widetilde{\boldsymbol{u}}^{n+1}+\widetilde{\boldsymbol{u}}^{n+1}\cdot\nabla\boldsymbol{u}^n-\nabla\cdot\left(2\nu\left(\boldsymbol{D}\boldsymbol{u}^n\right)\mathbf{D}\widetilde{\boldsymbol{u}}^{n+1}\right)+\nabla p^n &= \boldsymbol{f}^{n+1}+\boldsymbol{u}^n\cdot\nabla\boldsymbol{u}^n, \quad \text{in} \quad \Omega,\\
\widetilde{\boldsymbol{u}}^{n+1} &= \boldsymbol{g}_D^{n+1}, \quad \text{on} \quad \Gamma_D,\\
2\nu(\boldsymbol{D}\boldsymbol{u}^n)\boldsymbol{D}\widetilde{\boldsymbol{u}}^{n+1}\cdot\boldsymbol{n} &= p^n\boldsymbol{n}+\boldsymbol{g}_N^{n+1}, \quad \text{on} \quad \Gamma_N.
\end{aligned} \tag{12}$$

Step 2: Given $\widetilde{\boldsymbol{u}}^{n+1}$ from **Step 1**, compute the solution $\left(\boldsymbol{u}^{n+1}, p^{n+1}\right)$ of the Stokes problem as

$$\begin{aligned}
\frac{\boldsymbol{u}^{n+1}-\widetilde{\boldsymbol{u}}^{n+1}}{\Delta t}-\nabla\cdot\left(2\nu\left(\boldsymbol{D}\boldsymbol{u}^{n}\right)\left(\boldsymbol{D}\boldsymbol{u}^{n+1}-\mathbf{D}\widetilde{\boldsymbol{u}}^{n+1}\right)\right)+\nabla(p^{n+1}-p^{n}) &= 0, && \text{in } \Omega,\\
\nabla\cdot\boldsymbol{u}^{n+1} &= 0, && \text{in } \Omega,\\
\boldsymbol{u}^{n+1} &= \boldsymbol{g}_D^{n+1}, && \text{on } \Gamma_D,\\
\left(-p^{n+1}\boldsymbol{I}+2\nu\left(\boldsymbol{D}\boldsymbol{u}^{n}\right)\boldsymbol{D}\boldsymbol{u}^{n+1}\right)\cdot\boldsymbol{n} &= \boldsymbol{g}_N^{n+1}, && \text{on } \Gamma_N.
\end{aligned} \tag{13}$$

It should be noted that the main difference between the VS method (9)-(10) and the IVS method (12)-(13) lies in the addition of an extra explicit pressure term in each step, which is almost insignificant in terms of memory and computational cost. However, as shown by numerical simulations in Section 4, this adjustment has a significant improvement in the accuracy of the approximate solutions especially when tackling some severe situations like flow problems at high Reynolds number. It should also be stressed that recently, a similar approach but with different pressure correction strategy has been investigated in [58] for the Newtonian case.

3 Finite element method for spatial discretization

The starting point in the finite element method is the weak formulation of the equations (12)-(13). As in most finite element methods, this weak form is obtained by multiplying the equations (12)-(13) by a set of test functions and integrated over the domain Ω using the divergence theorem along with the boundary conditions. This yields:

Step 1: Given $(\boldsymbol{u}^n, p^n)$, find $\widetilde{\boldsymbol{u}}^{n+1}\in\mathbf{H}^1(\Omega)$ such that $\widetilde{\boldsymbol{u}}^{n+1}|_{\Gamma_D}=\boldsymbol{g}_D^{n+1}$, and for all $\boldsymbol{v}\in\mathbf{H}_0^1(\Gamma_D)$

$$\begin{aligned}
\int_\Omega\frac{\widetilde{\boldsymbol{u}}^{n+1}-\boldsymbol{u}^n}{\Delta t}\boldsymbol{v}\,d\boldsymbol{x}+\int_\Omega\boldsymbol{u}^n\cdot\nabla\widetilde{\boldsymbol{u}}^{n+1}\boldsymbol{v}\,d\boldsymbol{x}+\int_\Omega\widetilde{\boldsymbol{u}}^{n+1}\cdot\nabla\boldsymbol{u}^n\boldsymbol{v}\,d\boldsymbol{x}+\int_\Omega 2\nu(\boldsymbol{D}\boldsymbol{u}^n)\,\mathbf{D}\widetilde{\boldsymbol{u}}^{n+1}\boldsymbol{D}\boldsymbol{v}\,d\boldsymbol{x}=\\
\int_\Omega\boldsymbol{f}^{n+1}\boldsymbol{v}\,d\boldsymbol{x}+\int_\Omega\boldsymbol{u}^n\cdot\nabla\boldsymbol{u}^n\boldsymbol{v}\,d\boldsymbol{x}+\int_\Omega p^n\nabla\cdot\boldsymbol{v}\,d\boldsymbol{x}+\oint_{\Gamma_N}\boldsymbol{g}_N^{n+1}\boldsymbol{v}\,d\boldsymbol{x}.
\end{aligned} \tag{14}$$

Step 2: Given $\widetilde{\boldsymbol{u}}^{n+1}$, find $(\boldsymbol{u}^{n+1}, p^{n+1})\in\mathbf{H}^1(\Omega)\times L^2(\Omega)$, such that $\boldsymbol{u}^{n+1}|_{\Gamma_D}=\boldsymbol{g}_D^{n+1}$,
and for $(\boldsymbol{v}, q)\in\boldsymbol{H}_0^1(\Gamma_D)\times L^2(\Omega)$

$$\begin{aligned}
\int_\Omega\frac{\boldsymbol{u}^{n+1}-\widetilde{\boldsymbol{u}}^{n+1}}{\Delta t}\boldsymbol{v}\,d\boldsymbol{x}+\int_\Omega 2\nu(\boldsymbol{D}\boldsymbol{u}^n)\left(\boldsymbol{D}\boldsymbol{u}^{n+1}-\mathbf{D}\widetilde{\mathbf{u}}^{n+1}\right)\boldsymbol{D}\boldsymbol{v}\,d\boldsymbol{x}-\int_\Omega\left(p^{n+1}-p^n\right)\nabla\cdot\boldsymbol{v}\,d\boldsymbol{x} &= 0,\\
\int_\Omega\nabla\cdot\boldsymbol{u}^{n+1}q\,d\boldsymbol{x} &= 0.
\end{aligned} \tag{15}$$

Here, $\mathbf{H}^1(\Omega)$ is the well-known Sobolev space equipped with its usual norm denoted by $\|\cdot\|_1$, $L^2(\Omega)$ is the Lebesgue space of square-integrable functions supplied with its standard norm $\|\cdot\|$, and $\mathbf{H}_0^1(\Gamma_D)$ is a subspace of $\mathbf{H}^1(\Omega)$ defined as

$$\boldsymbol{H}_0^1(\Gamma_D)=\left\{\boldsymbol{v}\in\boldsymbol{H}^1(\Omega),\ \boldsymbol{v}|_{\Gamma_D}=0\right\},$$

and equipped with the semi-norm $|\boldsymbol{v}|_1=\|\nabla\boldsymbol{v}\|$. For the space discretization of $\overline{\Omega}=\Omega\cup\Gamma$, we generate a quasi-uniform partition $\Omega_h\subset\overline{\Omega}$ of elements $\mathcal{T}_k$ (triangles or quadrilaterals in two space dimensions, and tetrahedra or hexahedra in three space dimensions) such that $\overline{\Omega}=\cup_{k=1}^{N_e}\mathcal{T}_k$, where N_e is the number of elements of Ω_h, h is a space discretization parameter and the finite elements $\mathcal{T}_j$ satisfy, in the case of two-dimensional problems, the following conditions:

(i) $\overline{\Omega}=\bigcup_{j=1}^{Ne}\mathcal{T}_j$, where Ne is the number of elements of the partition Ω_h.

(ii) If $\mathcal{T}_i$ and $\mathcal{T}_j$ are two different elements of the partition Ω_h, then

$$\mathcal{T}_i \cap \mathcal{T}_j = \begin{cases} P_{ij}, & \text{a mesh point, or} \\ \Gamma_{ij}, & \text{a common side, or} \\ \emptyset, & \text{empty set.} \end{cases}$$

(iii) There exists a positive constant κ such that for all $j \in \{1, \ldots, Ne\}$, $\dfrac{d_j}{h_j} > \kappa$ $(h_j \leq h)$, where d_j is the diameter of the circle inscribed in $\mathcal{T}_j$ and h_j is the largest side of $\mathcal{T}_j$.

For the conforming finite element spaces for the velocity and pressure, we use the mixed Taylor-Hood $\mathbb{P}_2$-$\mathbb{P}_1$ finite elements *i.e.*, polynomials of second degree for the velocity and polynomials of first degree for the pressure. It is well known that for such elements the discrete velocity and pressure fields satisfy the inf-sup condition, see for instance [6]. The associated finite element spaces are defined as

$$\begin{aligned} V_h &= \Big\{ u_h \in C^0(\overline{\Omega}) : \quad u_h\big|_{\mathcal{T}_j} \in P_2(\mathcal{T}_j), \quad \forall\, \mathcal{T}_j \in \Omega_h \Big\}, \\ Q_h &= \Big\{ p_h \in C^0(\overline{\Omega}) : \quad p_h\big|_{\mathcal{T}_j} \in P_1(\mathcal{T}_j), \quad \forall\, \mathcal{T}_j \in \Omega_h \Big\}, \end{aligned}$$

where $P_2(\mathcal{T}_j)$ and $P_1(\mathcal{T}_j)$ are polynomial spaces defined in the element $\mathcal{T}_j$. Here, we define the finite element space $\mathbf{V}_h$ for the velocity field as $\mathbf{V}_h = V_h \times V_h$. Hence, we formulate the finite element solutions to $\boldsymbol{u}^n(\boldsymbol{x})$ and $p^n(\boldsymbol{x})$ as

$$\boldsymbol{u}_h^n(\boldsymbol{x}) = \sum_{j=1}^{M_u} \boldsymbol{U}_j^n \phi_j(\boldsymbol{x}), \qquad p_h^n(\boldsymbol{x}) = \sum_{k=1}^{M_p} P_k^n \psi_k(\boldsymbol{x}), \tag{16}$$

where M_u and M_p are respectively, the number of velocity and pressure mesh points in Ω_h. The functions $\boldsymbol{U}_j^n$ and P_k^n are the corresponding nodal values of $\boldsymbol{u}_h^n(\boldsymbol{x})$ and $p_h^n(\boldsymbol{x})$, respectively. They are defined as $\boldsymbol{U}_j^n = \boldsymbol{u}_h^n(\boldsymbol{x}_j)$ and $P_k^n = p_h^n(\boldsymbol{y}_k)$ where $\{\boldsymbol{x}_j\}_{j=1}^{M_u}$ and $\{\boldsymbol{y}_k\}_{k=1}^{M_p}$ are the set of velocity and pressure mesh points in Ω_h, respectively, so that $M_p < M_u$ and $\{\boldsymbol{y}_1, \ldots, \boldsymbol{y}_{M_p}\} \subset \{\boldsymbol{x}_1, \ldots, \boldsymbol{x}_{M_u}\}$. In (16), $\{\phi_j\}_{j=1}^{M_u}$ and $\{\psi_l\}_{k=1}^{M_p}$ are respectively, the set of global nodal basis functions of the velocity and the pressure characterized by the property $\phi_i(\boldsymbol{x}_j) = \delta_{ij}$ and $\psi_i(\boldsymbol{y}_k) = \delta_{il}$ with δ denoting the Kronecker symbol. Next, the discrete weak formulation of (14)-(15) reads:

Step 1: Solve for $\widetilde{\boldsymbol{u}}_h^{n+1} \in \boldsymbol{V}_h$, such that for all $\boldsymbol{v}_h \in \boldsymbol{V}_h$ with $\boldsymbol{v}_h|_{\Gamma_D} = 0$

$$\begin{aligned} \int_{\Omega_h} \frac{1}{\Delta t} \widetilde{\boldsymbol{u}}_h^{n+1} \cdot \boldsymbol{v}_h d\boldsymbol{x} + \int_{\Omega_h} (\boldsymbol{u}_h^n \cdot \nabla \widetilde{\boldsymbol{u}}_h^{n+1}) \cdot \mathbf{v_h} d\boldsymbol{x} + \int_{\Omega_h} (\widetilde{\boldsymbol{u}}_h^{n+1} \cdot \nabla \boldsymbol{u}_h^n) \cdot \boldsymbol{v}_h d\boldsymbol{x} + \\ \int_{\Omega_h} 2\nu(\boldsymbol{D}\boldsymbol{u}_h^n) \mathbf{D}\widetilde{\boldsymbol{u}}_h^{n+1} \colon \boldsymbol{D}\boldsymbol{v}_h d\boldsymbol{x} = \int_{\Omega_h} p_h^n \nabla \cdot \boldsymbol{v}_h d\boldsymbol{x} + \int_{\Omega_h} \frac{1}{\Delta t} \boldsymbol{u}_h^n \cdot \boldsymbol{v}_h d\boldsymbol{x} + \int_{\Omega_h} \boldsymbol{f}^{n+1} \cdot \boldsymbol{v}_h d\boldsymbol{x} + \\ \int_{\Omega_h} (\boldsymbol{u}_h^n \cdot \nabla \boldsymbol{u}_h^n) \cdot \boldsymbol{v}_h d\boldsymbol{x} + \int_{\Gamma_N} \boldsymbol{g}_N^{n+1} \cdot \boldsymbol{v}_h d\Gamma. \end{aligned} \tag{17}$$

Step 2: Solve the Stokes problem for $(\boldsymbol{u}_h^{n+1}, p_h^{n+1}) \in \boldsymbol{V}_h \times Q_h$, such that for all $(\boldsymbol{v}_h, q_h) \in \boldsymbol{V}_h \times Q_h$ with $\boldsymbol{v}_h^{n+1}|_{\Gamma_D} = \mathbf{0}$

$$\begin{aligned} \int_{\Omega_h} \frac{1}{\Delta t} \boldsymbol{u}_h^{n+1} \cdot \boldsymbol{v}_h d\boldsymbol{x} + \int_{\Omega_h} 2\nu(\boldsymbol{D}\boldsymbol{u}_h^n) \boldsymbol{D}\boldsymbol{u}_h^{n+1} \colon \boldsymbol{D}\boldsymbol{v}_h d\boldsymbol{x} - \int_{\Omega_h} p_h^{n+1} \nabla \cdot \boldsymbol{v}_h d\boldsymbol{x} = \\ \int_{\Omega_h} \frac{1}{\Delta t} \widetilde{\boldsymbol{u}}_h^{n+1} \cdot \boldsymbol{v}_h d\boldsymbol{x} + \int_{\Omega_h} 2\nu(\boldsymbol{D}\boldsymbol{u}_h^n) \mathbf{D}\widetilde{\mathbf{u}}_h^{n+1} \colon \boldsymbol{D}\boldsymbol{v}_h d\boldsymbol{x} + \int_{\Omega_h} p_h^n \nabla \cdot \boldsymbol{v}_h d\boldsymbol{x}, \\ \int_{\Omega_h} q_h \nabla \cdot \boldsymbol{u}_h^{n+1} d\boldsymbol{x} = 0. \end{aligned} \tag{18}$$

Algorithm 1: Improved viscosity-splitting algorithm.

Initialization: set $n = 0$, $\boldsymbol{u}^0 = \boldsymbol{u}_0$, $p^0 = p_0$ where p_0 is an initial pressure, for example $p_0 = 0$, a tolerance ϵ and a maximum number of steps N_{max};
while $n \leq N_{max}$ **do**
  Compute $\widetilde{\boldsymbol{u}}^{n+1}$ through the equation (17);
  Compute $(\boldsymbol{u}^{n+1}, p^{n+1})$ by solving (18);
  Convergence test: compute, for example, the relative L^2-error $err = \dfrac{\|\boldsymbol{u}^{n+1} - \boldsymbol{u}^n\|}{\|\boldsymbol{u}^{n+1}\|}$;
  if $err < \epsilon$ **then**
    Stop
  else
    $p^n \leftarrow p^{n+1}$;
    $\boldsymbol{u}^n \leftarrow \boldsymbol{u}^{n+1}$;
    Set $n \leftarrow n + 1$;
    Go to 2
  end
end

Using the finite element approximations in (16), the fully discrete formulation of (17) and (18) results in two linear systems of the following form

$$\left(\frac{1}{\Delta t}\mathbf{M} + \mathbf{N}(\boldsymbol{u}^n) + \mathbf{K}(\boldsymbol{u}^n)\right)\widetilde{\boldsymbol{U}}^{n+1} = \widetilde{\mathbf{F}}(\boldsymbol{u}^n), \tag{19}$$

and

$$\begin{pmatrix} \frac{1}{\Delta t}\mathbf{M} + \mathbf{K}(\boldsymbol{u}^n) & \mathbf{B}^T \\ \mathbf{B} & \mathbf{0} \end{pmatrix} \begin{pmatrix} \boldsymbol{U}^{n+1} \\ P^{n+1} \end{pmatrix} = \begin{pmatrix} \mathbf{F}(\boldsymbol{u}^n) \\ \mathbf{0} \end{pmatrix}, \tag{20}$$

respectively. Here, $\boldsymbol{U}^{n+1}$, $\widetilde{\boldsymbol{U}}^{n+1}$ and P^{n+1} are respectively, M_u-valued and M_p-valued vectors with unknowns entries $\boldsymbol{U}_j$, $\widetilde{\boldsymbol{U}}_j$ and P_k ($j = 1, \ldots, M_u$ and $k = 1, \ldots, M_p$) as defined in (16), $\mathbf{M}$, $\mathbf{N}$, $\mathbf{K}$ are squared $M_u \times M_u$-valued matrices and $\mathbf{B}$ is a squared $M_p \times M_p$-valued matrix whose elements entries are respectively given by

$$M_{ij} = \int_{\Omega_h} \phi_j \phi_i d\boldsymbol{x}, \qquad N_{ij} = \int_{\Omega_h} (\boldsymbol{u} \cdot \nabla \phi_j) \cdot \phi_i + \int_{\Omega_h} (\phi_j \cdot \nabla \boldsymbol{u}) \cdot \phi_i d\boldsymbol{x},$$

$$K(\boldsymbol{u})_{ij} = \int_{\Omega_h} 2\nu(\boldsymbol{D}\boldsymbol{u})\boldsymbol{D}\phi_j : \boldsymbol{D}\phi_i d\boldsymbol{x}, \qquad B_{ij} = -\int_{\Omega_h} \psi_i \nabla \cdot \phi_j d\boldsymbol{x}.$$

In (19)-(20), $\widetilde{\mathbf{F}}(\boldsymbol{u}^n)$ and $\mathbf{F}(\boldsymbol{u}^n)$ are M_u-valued vectors with entries

$$\widetilde{\boldsymbol{F}}(\boldsymbol{u})_j = (\boldsymbol{B}P^n)_j + \frac{1}{\Delta t}(\boldsymbol{M}\boldsymbol{U}^n)_j + \int_{\Omega_h} \boldsymbol{f}^{n+1}\phi_j d\boldsymbol{x} + \int_{\Omega_h} (\boldsymbol{u} \cdot \nabla \boldsymbol{u})\phi_j d\boldsymbol{x} + \int_{\Gamma_N} \boldsymbol{g}_N^{n+1}\phi_j d\boldsymbol{x},$$

and

$$\mathbf{F}(\boldsymbol{u}) = \left(\frac{1}{\Delta t}\mathbf{M} + \boldsymbol{K}(\boldsymbol{u})\right)\widetilde{\boldsymbol{U}}^{n+1} + \boldsymbol{B}P^n.$$

Note that when $\Gamma_D = \partial\Omega$, (*i.e.* $\Gamma_N = \emptyset$) and the Dirichlet boundary condition is imposed over all the domain boundaries, the pressure solution becomes only unique up to an additional constant. To ensure the uniqueness of this solution, we impose a zero-mean condition on the pressure *i.e.* $p \in L_0^2(\Omega)$ which is numerically implemented through the additional step as

$$p_h^{n+1} \longleftarrow p_h^{n+1} - \frac{1}{|\Omega_h|}\int_{\Omega_h} p_h^{n+1} d\boldsymbol{x}. \tag{21}$$

For completeness, improved viscosity-splitting algorithm is detailed in Algorithm 1. Some remarks are in order:

i. The system matrix in (20) can be rewritten in a compact form as

$$\mathcal{A} = \begin{pmatrix} \boldsymbol{A} & \boldsymbol{B}^T \\ \boldsymbol{B} & \mathbf{0} \end{pmatrix}, \tag{22}$$

with $\boldsymbol{A} = \dfrac{1}{\Delta t}\mathbf{M}+\mathbf{K}(\boldsymbol{u}^n)$. Here, the $\mathcal{A}$ is symmetric but indefinite according to the Sylvester law of inertia (see [29], p:403) whereas the matrix $\boldsymbol{A}$ is symmetric and positive definite. In this case, the well-established Krylov subspace methods can be of good choice but preconditioning is essential since the saddle-point systems arising from the finite element discretization are usually challenging to solve in practice.

ii. Although the system (20) is only symmetric and not positive definite, it is still possible, using a proper block preconditioner and a non-standard inner product, to apply the efficient conjugate gradient method. In fact, an interesting approach presented in [7] proposes a block triangular preconditioner of the form

$$\begin{pmatrix} \boldsymbol{A}-\boldsymbol{A}_0 & 0 \\ \boldsymbol{B} & -\boldsymbol{I} \end{pmatrix},$$

where $\boldsymbol{A}_0$ is a symmetric positive definite matrix such that $\boldsymbol{A}-\boldsymbol{A}_0$ is also symmetric positive definite. Note that an obvious choice in our case would be $\boldsymbol{A}_0 = \dfrac{1}{\Delta t}\boldsymbol{M}$. It was shown that the resulting preconditioned matrix is also symmetric positive definite with respect to the inner product defined by

$$\langle x, y\rangle_{\mathcal{H}} = x^T\mathcal{H}y, \qquad \text{with} \qquad \mathcal{H} = \begin{pmatrix} \boldsymbol{A}-\boldsymbol{A}_0 & \mathbf{0} \\ \mathbf{0} & \boldsymbol{I} \end{pmatrix}.$$

In all our computations the resulting linear systems of algebraic equations (19) and (20) were solved using a preconditioned conjugate gradient solver with incomplete Cholesky decomposition and a tolerance of 10^{-6} to stop the iterations. For all considered flow regimes in the present work, the number of iterations to reach this tolerance does not exceed 100 iterations.

4 Numerical results and examples

In this section, the accuracy of the improved viscosity-splitting method (IVS) introduced in the above sections is assessed using test examples of unsteady generalized Newtonian fluid flow problems. In the first example, quantitative results are examined for a three-dimensional problem with known analytical solutions. The second and third examples examine the performance of the proposed method for solving the well-established benchmark problems of lid-driven cavity flow and flow past a circular cylinder. Comparisons between results obtained using both conventional and improved viscosity-splitting methods are presented for the considered problems.

4.1 Accuracy example

We first assess the numerical accuracy of the proposed improved viscosity-splitting method by solving the equations (1)-(3) equipped with a manufactured exact solution. The equations are solved in a three-dimensional

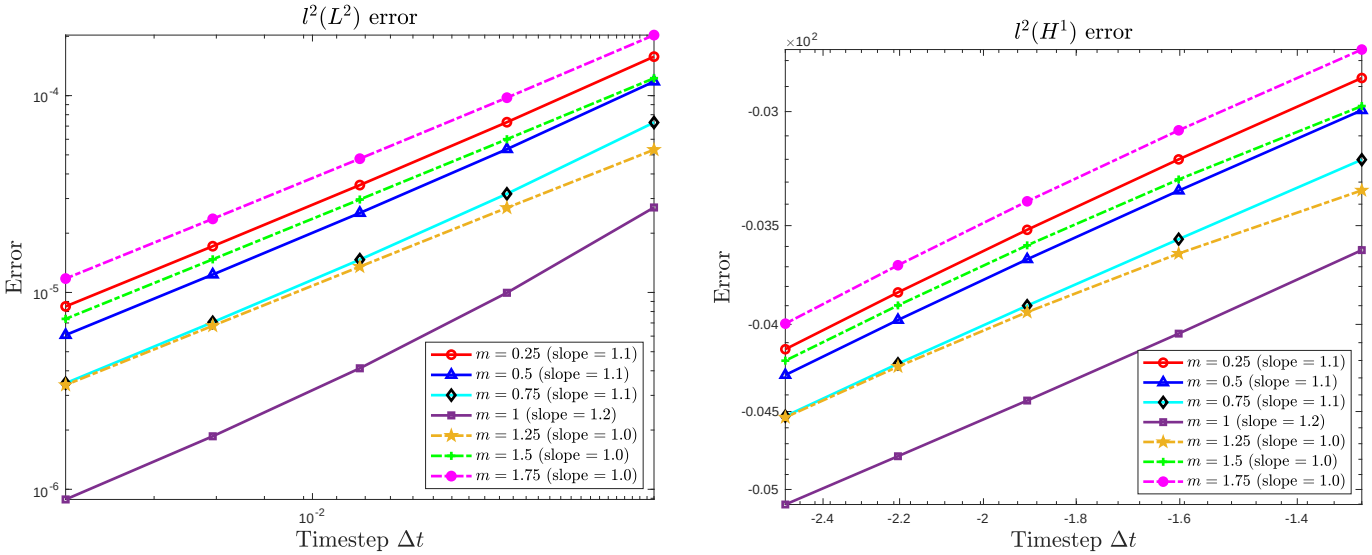

Figure 1: Convergence results obtained for the velocity solution in the accuracy example using the IVS method with different fluid cases.

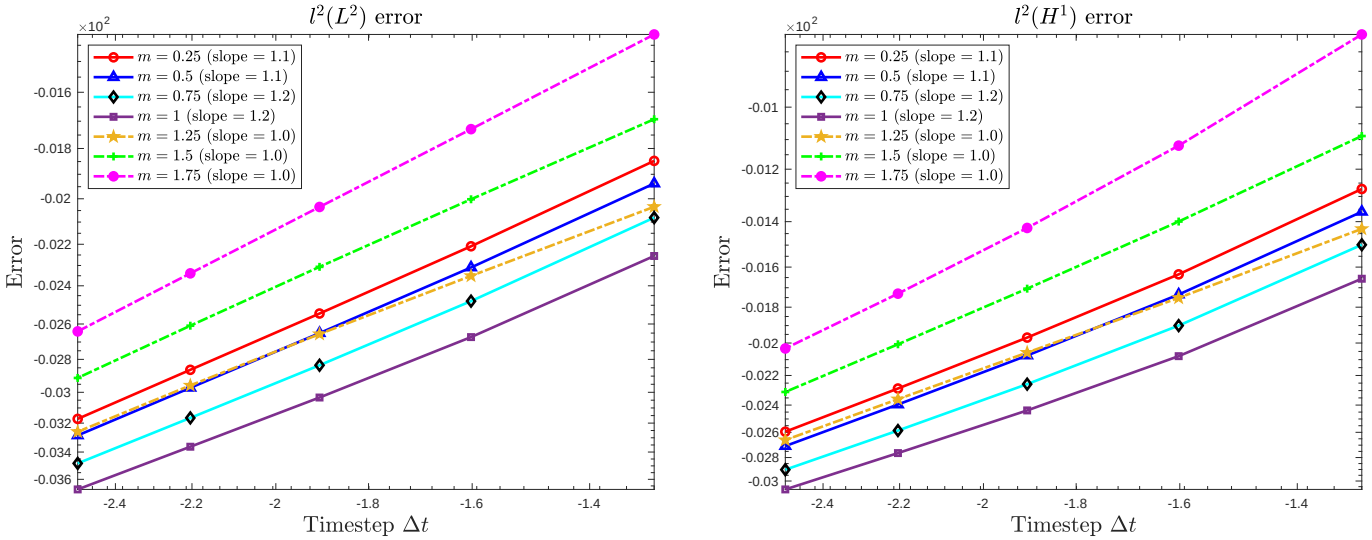

Figure 2: Convergence results obtained for the pressure solution in the accuracy example using the IVS method with different fluid cases.

domain $\Omega = [0,1] \times [0,1] \times [0,1]$ subject to homogeneous Dirichlet-type boundary conditions and the function $\mathbf{f}(t,x,y,z)$ is defined such that the analytical solution of (1)-(3) is defined as

$$\begin{aligned} \boldsymbol{u}(t,x,y,z) &= \left(x + x^2 + xy + xz, y + y^2 - xy - 3yz, -2z + z^2 - xz - 3yz\right)^\top \sin(t), \\ p(t,x,y,z) &= (x - y + z)\sin(t). \end{aligned} \tag{23}$$

The Carreau constitutive relation (3) is considered for this example with

$$\nu_\infty = 0.01, \qquad \nu_0 = 1, \qquad C_0 = 1, \qquad \lambda = 1,$$

and different values of the power index m which has the key role in defining the rheology of fluids under study (*i.e.* Newtonian, shear-thinning, shear-thickening). To quantify the convergence rates of the viscosity-splitting

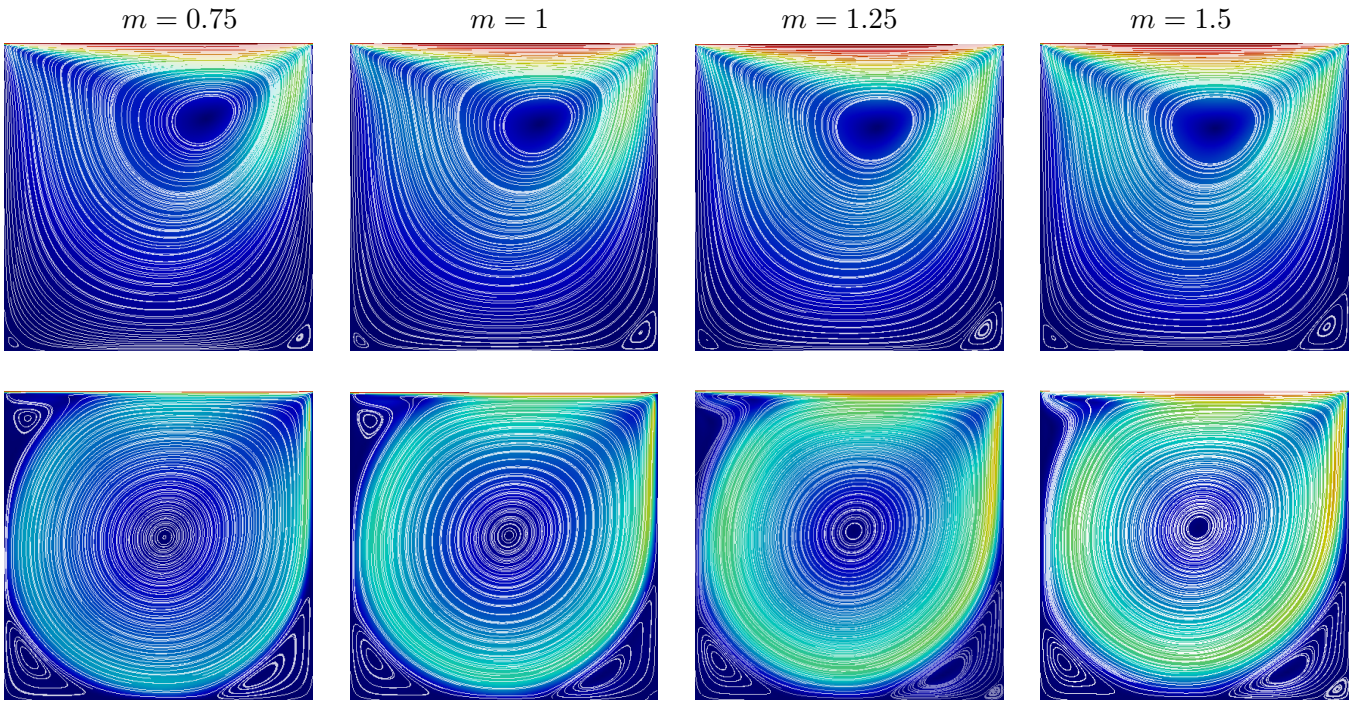

Figure 3: Streamlines and velocity magnitudes for the lid-driven cavity flow at $Re = 100$ (first row) and $Re = 5000$ (second row) obtained using the IVS method with different values of the index m. Here, $m = 0.75$ (first column), $m = 1$ (second column), $m = 1.25$ (third column) and $m = 1.5$ (fourth column).

method, we compute the errors between the numerical and exact solutions using the following norm

$$\|\mathbf{e}\|_{l^2(\mathbf{X})} = \left(\Delta t \sum_{n=0}^{N} \|\mathbf{e}^n\|_{\mathbf{X}}^2 \right)^{1/2},$$

where $\mathbf{X}$ is taken as $\left(L^2(\Omega)\right)^3$ or $\left(H^1(\Omega)\right)^3$ for the velocity solution, and as $L^2(\Omega)$ or $H^1(\Omega)$ for the pressure solution. Notice that, since the objective of this test example is to study the time convergence, it is desirable to strongly reduce any spacial errors. Therefore, as $\mathbb{P}_2$-$\mathbb{P}_1$ finite elements are used for the spatial discretization, the analytical solution (23) is selected to be quadratic polynomials for the velocity and a linear polynomial for the pressure with respect to the space variable. In the framework of Newtonian fluid flows with constant viscosity, this choice would completely remove the spatial component of the error even with a coarser mesh, allowing a better evaluation of errors in the time integration procedure.

In all simulations presented for this example, a uniform structured finite element mesh with $10 \times 10 \times 10$ elements is used, different time steps defined by $\Delta t = \dfrac{0.1}{2^n}$ (with $n = 1, \ldots, 5$) and the computed results are presented at the final time $t = 0.5$. In Figure 1 we display the convergence plots obtained for the velocity field using the considered norms and different values of the power index m in the constitutive law (3) namely $m = 0.25$, 0.5, 0.75, 1, 1.25, 1.5 and 1.75 which correspond to different classes of the fluid under study. Those convergence plots obtained for the pressure solution are illustrated in Figure 2. For the considered test cases, it is clear that the method is first-order accurate for both the velocity and pressure approximations in the norms $\boldsymbol{L}^2(0,T;\boldsymbol{L}^2(\Omega))$ and $\boldsymbol{L}^2(0,T;\boldsymbol{H}^1(\Omega))$. In addition, this convergence order is also maintained regardless of the fluid class *i.e.* Newtonian ($m = 1$), shear-thinning ($m < 1$) or shear-thickening ($m > 1$), but with a slight change in the error magnitude depending on the value of the power index m. Here, the error decreases as the fluid changes from the shear-thinning case ($m < 1$) to the shear-thickening case ($m > 1$). For these cases, we obviously notice that the error plots keep the same trends and these results also demonstrate that the proposed IVS method is suited for the numerical solution of unsteady generalized Newtonian fluid flow problems.

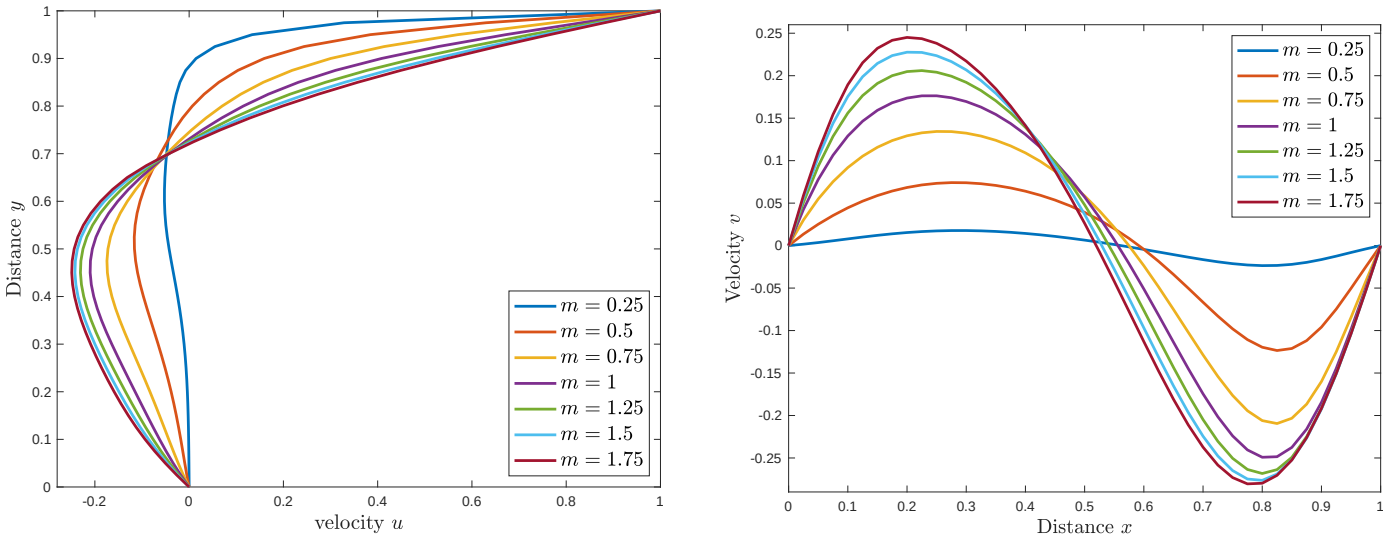

Figure 4: Velocity profiles for u (left) and v (right) through the geometric center of the cavity for the lid-driven cavity flow at $Re = 100$ obtained using the IVS method with different values of the index m.

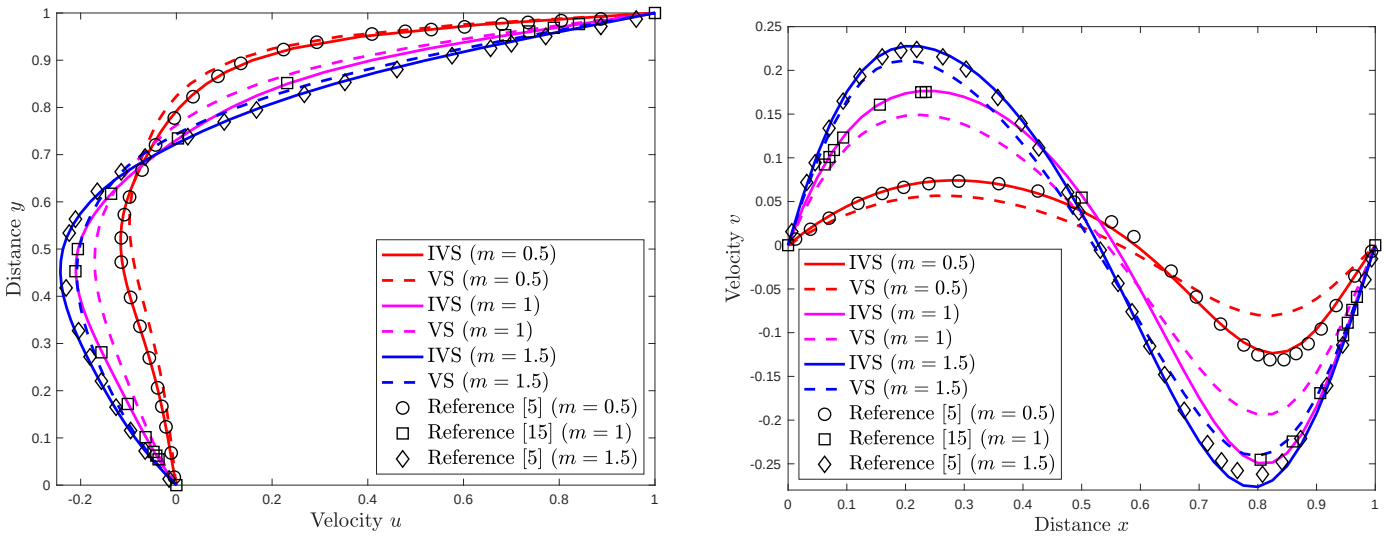

Figure 5: Velocity profiles for u (left) and v (right) through the geometric center of the cavity for the lid-driven cavity flow at $Re = 100$ obtained using the VS and IVS methods with different values of the index m.

4.2 Lid-driven cavity flow

In this test example, we consider the canonical problem of a lid-driven cavity flow first studied in [1, 25, 8] among others, and it is widely used in the literature to validate numerical methods for incompressible Navier-Stokes equations mainly due to its simple setup and rich flow patterns. The problem consists of a squared cavity of length L filled of a fluid satisfying the power law

$$\mu(\boldsymbol{Du}) = \nu_0 \left(|\boldsymbol{Du}|\right)^{m-1},$$

where ν_0 is the consistency parameter and m the dimensionless power index. Note that $m > 1$ corresponds to a shear-thickening fluid and $m < 1$ represents a shear-thinning fluid, while $m = 1$ covers the Newtonian fluids. The vertical and bottom walls of the cavity are fixed whereas the upper lid is driven at a constant velocity u_∞ in the horizontal direction. Hence, the Reynolds number which characterizes the overall flow behavior is defined by $Re = \frac{u_\infty^{2-m} L^m}{\nu_0}$. In our simulations, we use $L = 1$, $u_\infty = 1$, the Reynolds number is set to $Re = 100$

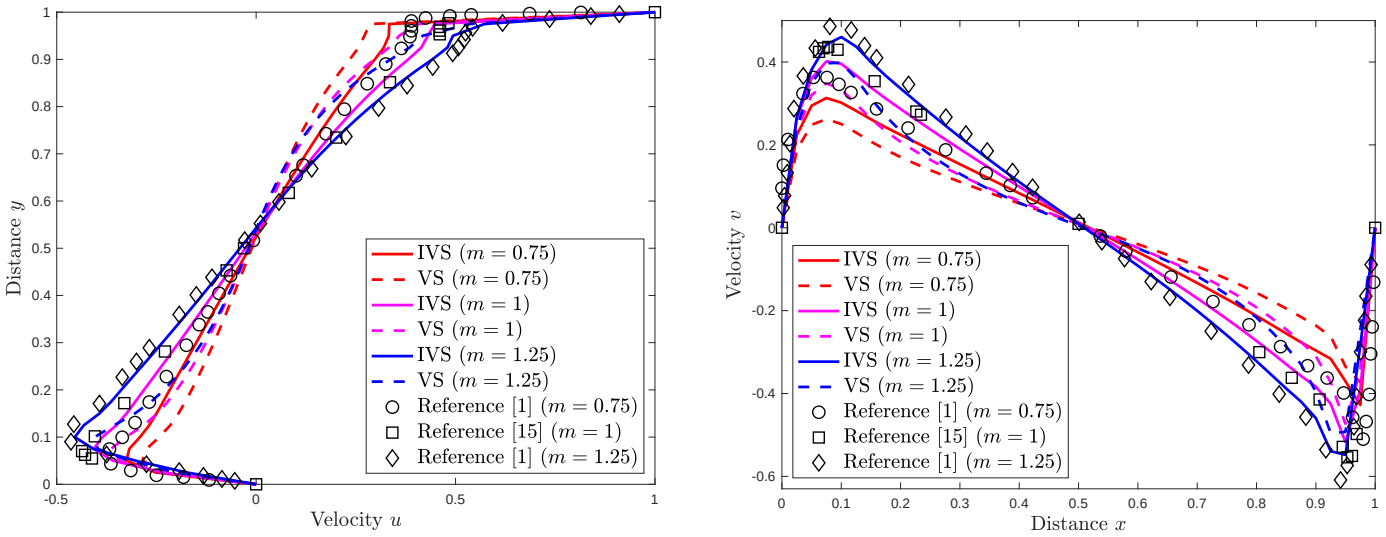

Figure 6: Velocity profiles for u (left) and v (right) through the geometric center of the cavity for the lid-driven cavity flow at $Re = 5000$ obtained using the VS and IVS methods with different values of the index m.

and $Re = 5000$ for which $\nu_0 = \frac{u_\infty^{2-m}}{Re}$ is adjusted according to the selected power index m in order to reach the Reynolds number of interest. The computational domain is discretized using an unstructured mesh of 904 elements with 549 pressure nodes and 2001 velocity nodes. The time step Δt is fixed to 0.05 and steady-state solutions are presented. In all results presented here, the time stepping was terminated when the relative difference between two consecutive computed solutions in L^2-norm is less than a tolerance of 10^{-6}.

Table 1: Numbers of time steps in the VS and IVS methods for the lid-driven cavity flow at $Re = 100$ and $Re = 5000$ with different values of the index m.

	$Re = 100$				$Re = 5000$			
	$m = 0.75$	$m = 1$	$m = 1.25$	$m = 1.5$	$m = 0.75$	$m = 1$	$m = 1.25$	$m = 1.5$
VS	177	171	120	97	32754	23667	15428	14173
IVS	213	202	129	99	46122	43384	30390	24318

We first consider the case with $Re = 100$ and $Re = 5000$ using different values of the power index m, namely $m = 0.25$, 0.75, 1, 1.25, 1.5 and 1.75. In Figure 3 we display the streamlines obtained using the proposed IVS method for $m = 0.75$, 1, 1.25 and 1.5. Notice that the colors in these figures refer to the velocity magnitude for each flow regime. The obtained results exhibit a clear view of the overall flow patterns and the effects of the power index on the structures of steady recirculating eddies in the cavity. In addition to the primary center vortex, a pair of counter-rotating eddies of a much smaller strength are developed in the lower corners of the cavity. It is also noticeable that the size of these eddies increases as the power index m increases for a fixed Reynolds number. Here, the streamlines in Figure 3 exhibit the typical behavior of the lid-driven cavity flow influenced by the Reynolds number as we can clearly observe the formation of a series of secondary vortices (see left and right bottom corners of the cavity) at $Re = 100$ in addition to the third secondary vortex (see left top corner of the cavity) and the tertiary vortices (see left and right bottom corners of the cavity) emerging as the Reynolds number increases to $Re = 5000$. Notice that, when it comes to the non-Newtonian case, the usual behavior may be derailed under the effect of the power index m. For example at $Re = 5000$ and as m increases, the vortex at the left top corner shrinks while the tertiary vortices at left and right bottom corners become bigger and push inward the secondary vortices located at the bottom, the size of which gets enlarged as well. The effect of the power index m is further illustrated locally by the velocity profiles along the vertical

and horizontal centerlines in Figure 4. It is clear that, for the same fixed Reynolds number, the shear-thinning fluids (with $m < 1$) are exhibiting a less larger and more sharper velocity profiles than the dilatant fluids (with $m > 1$), demonstrating a greater reaction towards changes in the shear-rate stresses near the walls, which is compatible with their physical features.

Next, we compare the results obtained using the proposed IVS method and those obtained using the conventional VS method. To this end, we illustrate in Figure 5 the velocity profiles along the vertical and horizontal centerlines obtained using the IVS and VS methods at $Re = 100$ with $m = 0.5$, 1 and 1.5. Those results obtained using the IVS and VS methods at $Re = 5000$ with $m = 0.75$, 1 and 1.25 are presented in Figure 6. For comparison reasons, we also include in these figures the well-established results from the literature [25] for $Re = 100$ and $Re = 5000$ with $m = 1$, [8] for $Re = 100$ with $m = 0.5$ and $m = 1.5$, and [1] for $Re = 5000$ with $m = 0.75$ and $m = 1.25$. As expected, the velocity profiles change from curved at the low value of $Re = 100$ to linear at the high value $Re = 5000$. Clearly, the velocity profiles obtained using the proposed IVS method are more accurate than those obtained using the conventional VS method and agree well with the results published in the literature for the considered Reynolds numbers and power indices. This confirms the better performance achieved by the proposed IVS method compared to the standard VS method when solving this class of lid-driven cavity flow. For the considered fluid regimes, it can be clearly seen that the complicated flow structures are well captured by the proposed IVS method. In fact, the computed solutions reveal the physics well in this test example for unsteady generalized Newtonian fluid flow problems.

As a final remark for this test example, we comment on the number of time steps required in the VS and IVS methods to reach the steady-state solutions for the considered Reynolds numbers and power indices. In Table 1 we summarize the number of time steps required for each method solving the lid-driven cavity flow at $Re = 100$ and $Re = 5000$ using different values of the power index m, namely $m = 0.75$, 1, 1.25 and 1.5. It is clear that for a fixed Reynolds number, the number of time steps decreases as the power index m increases in both methods but the proposed IVS method requires a larger number of steps than its conventional counterpart for all selected Reynolds numbers. However, given the far better quality of the solution computed using the IVS method as shown previously, this lower number of time steps required by the VS method is due to its incapability to provide improved approximations throughout the time integration procedure. In fact, given a severe flow situation (such as $Re = 5000$) where the steady-state solutions can not be reached easily, the VS method just stagnates after a certain number of steps and its future approximations will be so close to the actual ones announcing its convergence, even if the flow is still developing. On the contrary, the IVS method keeps improving its approximations until the expected steady-state solutions are reached. This is also supported by the fact that at $Re = 100$ which corresponds to a relatively smooth flow compared to the flow at $Re = 5000$), the difference in the number of time steps is mediocre. It should also be pointed out that most of the computational effort goes into solving the linear systems in the IVS method. Therefore, reducing the computational cost in the viscosity-splitting method can be achieved by implementing a more efficient preconditioned iterative solver for these linear systems. For instance, multigrid techniques are well known to be among most efficient methods for solving linear systems and can therefore be the suitable tools to increase the efficiency of the viscosity-splitting method.

4.3 Flow past a circular cylinder

In this example we consider a more complex problem which involves the flow of a viscous fluid past a circular cylinder. This is a well established flow benchmark widely used in the literature to assess numerical methods in computational fluid dynamics, see for instance [39, 12, 13, 14, 31]. In our computations for this example we used the same flow configuration and the same boundary conditions as detailed in the previous references. Thus, the computational domain consists of a squared geometry of length $L = 100D$ containing a circular cylinder of diameter $D = 1$ positioned at the point $(19.5, 50)^\top$ of the Cartesian coordinates as shown in Figure 7. Using the boundary notation defined in Figure 7, Dirichlet-type boundary conditions are used for the velocity on Γ_D, a homogeneous Neumann condition is imposed at the outlet boundary Γ_N, and a no-slip condition is enforced at the cylinder boundary Γ_C as

$$\boldsymbol{u} = (u_\infty, 0)^\top, \quad \text{on } \Gamma_D, \qquad \boldsymbol{u} = \boldsymbol{0}, \quad \text{on } \Gamma_C \qquad \text{and} \qquad \sigma(\boldsymbol{u})\mathbf{n} = \boldsymbol{0}, \quad \text{on } \Gamma_N.$$

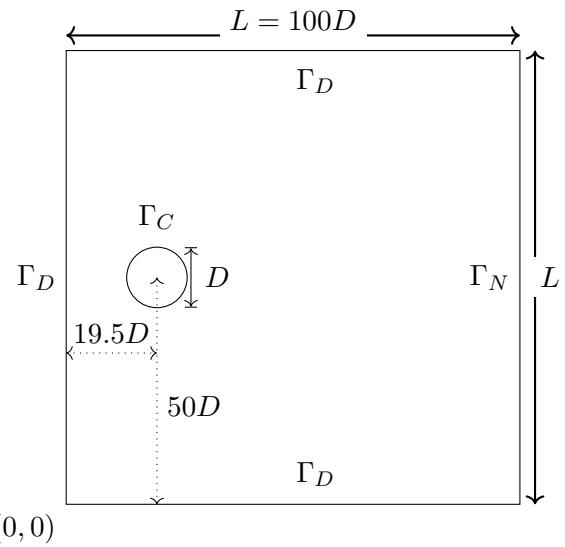

Figure 7: Configuration of the domain for the flow problem past a circular cylinder.

In this example, the Carreau-Yoshida viscosity model (3) is used here with $C_0 = 1$ as

$$\nu(\boldsymbol{Du}) = \nu_\infty + (\nu_0 - \nu_\infty)\left(1 + \lambda^2 \|\boldsymbol{Du}\|^2\right)^{\frac{m-1}{2}},$$

where $\nu_0 = 0.1$ and $\nu_\infty = 0.001$. Hence, the Reynolds number Re and the Carreau number C_U characterizing the flow are defined by

$$Re = \frac{\rho D u_\infty}{\nu_0}, \qquad C_U = \frac{\lambda u_\infty}{D},$$

where $u_\infty = 1$ is the maximum inflow velocity, and $\rho = 1kg/m^3$ is the fluid density. We perform numerical simulations for the Reynolds number $Re = 10$ with the Carreau numbers $C_U = 10$ and $C_U = 20$ using a power index m ranging from 0.1 to 1.9 which covers a wide spectrum of non-Newtonian fluid flows. Based on a mesh convergence study not reported here for brevity, an unstructured triangular mesh of 14007 mixed elements with 7105 pressure nodes and 28138 velocity nodes is used in our simulations as it offers a compromise between accuracy and efficiency in the IVS method. Using the same procedure as in the previous test example, the time step $\Delta t = 0.1$ and steady-state solutions are presented. Note that thanks to the availability of well documented results, this example enables us to precisely evaluate the proposed IVS method based on local physical quantities of interest like the length of the recirculation region measured along the centerline axis between the cylinder back base point and the stagnation point downstream.

Figure 8, Figure 9 and Figure 10 depict the streamlines and velocity magnitudes obtained using the selected Reynolds number $Re = 10$ and the Carreau numbers $C_U = 10$ with $C_U = 20$ for the shear-thinning ($m < 1$), Newtonian ($m = 1$) and shear-thickening ($m > 1$) fluids, respectively. For a better insight, only the focused area $[18, 28] \times [47, 52]$ of the computational domain is displayed in these figures to clearly illustrate the flow features around the cylinder and the region behind it. As it can be seen from these figures, the flow reaches a steady state with a clear symmetry with respect to the horizontal centerline for all selected fluid regimes. From the same figures we can also observe the variation in the size of wake zones under the influence of the power index m and the Carreau number C_U. For example, at the same Reynolds and Carreau numbers, the recirculation region becomes longer as the power index m decreases, with a more important horizontal expansion in the case of shear-thinning fluids. Indeed, for the Newtonian case (with $m = 1$) at the low Reynolds number, the fluid near the forward half of the cylinder gets accelerated until it reaches the top and bottom of the cylinder, then its velocity begins to drop and the pressure starts to increase. This rise in the pressure creates an adverse pressure gradient acting on the fluid within the boundary layer where more viscous effects are experienced (due to the no-slip boundary condition) and more energy dissipation occurs yielding the inability of the fluid near the wall to resist this adverse pressure force. Consequently, the flow is completely reversed and confined in a

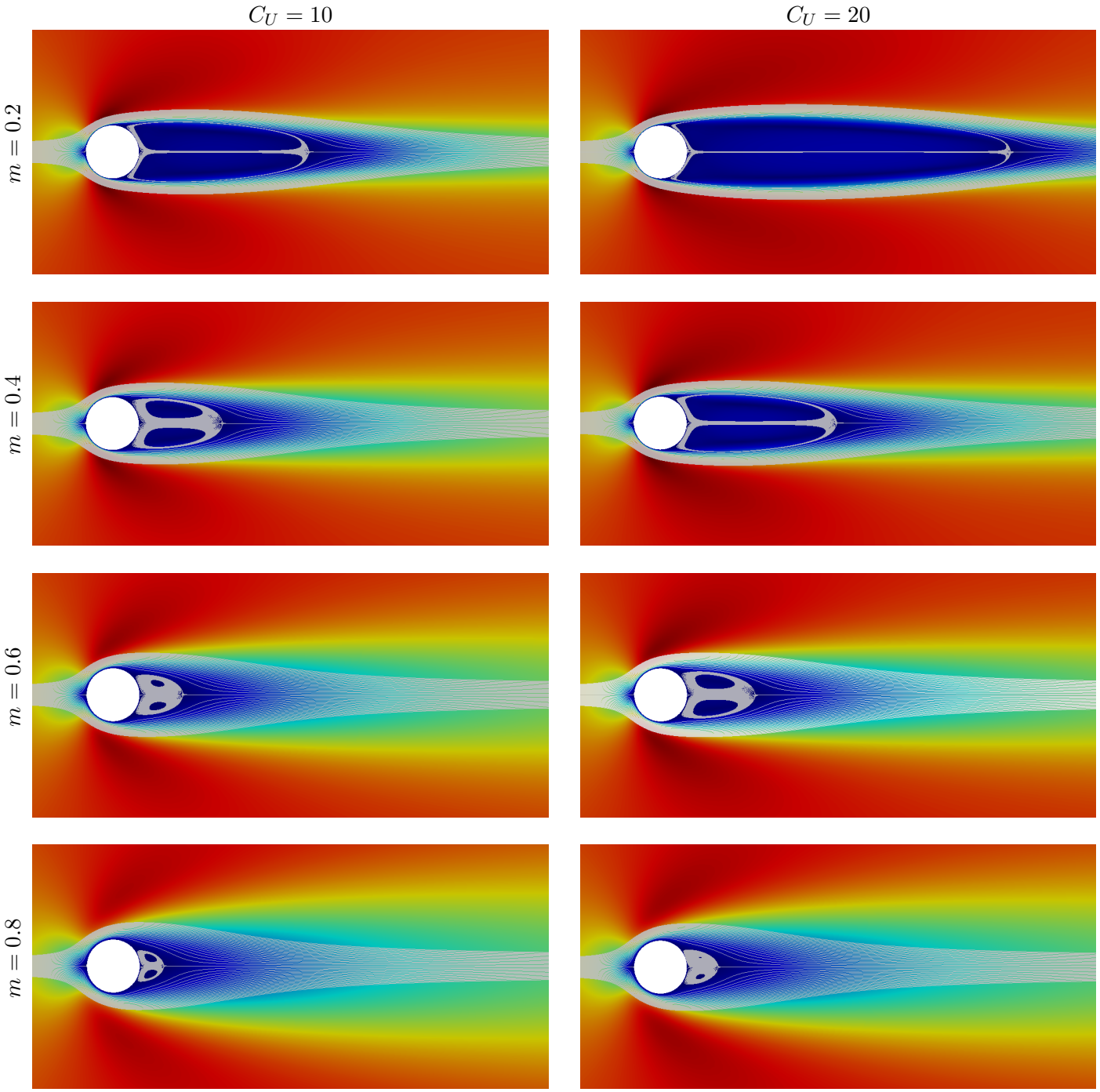

Figure 8: Streamlines and velocity magnitudes for the flow past a circular cylinder at Carreau numbers $C_U = 10$ (first column) and $C_U = 20$ (second column) obtained using the IVS method for shear-thinning fluids with $m = 0.2$ (first row), $m = 0.4$ (second row), $m = 0.6$ (third row) and $m = 0.8$ (fourth row).

pair of axisymmetric eddies in which the fluid is separated from the main flow and it recirculates with a lower velocity.

As the power index m decreases below 1, and due to the shear-thinning effects, the viscosity drops considerably around the recirculation zone since the shear rates in this region are large (streamlines are closer to each other in this region). Consequently, according to [39], a reduction in the shear stress occurs which in turn decreases the entrainment of fluids from the main stream to the wake allowing the wake bubble to get stretched and to become wider as observed in the streamlines shown in Figure 8. On the other hand, when

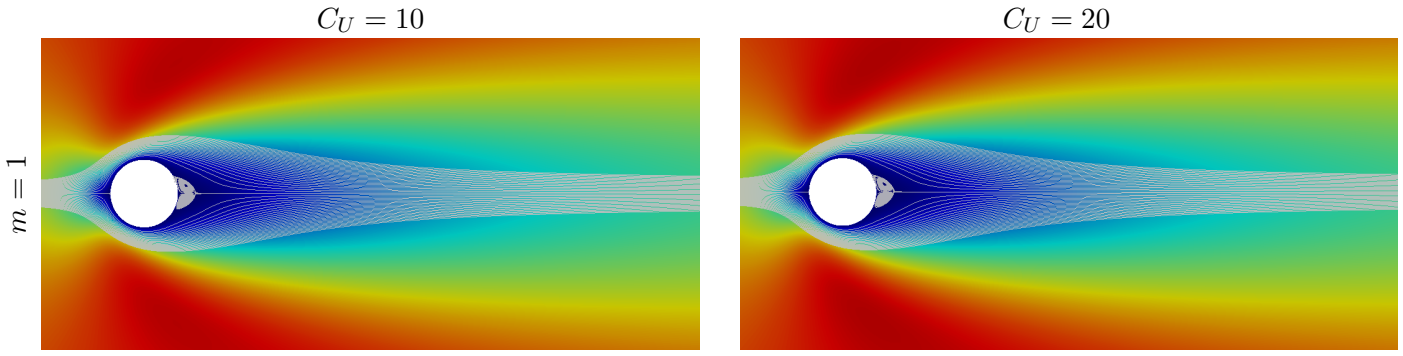

Figure 9: Streamlines and velocity magnitudes for the flow past a circular cylinder at Carreau numbers $C_U = 10$ (first column) and $C_U = 20$ (second column) obtained using the IVS method for Newtonian fluids with $m = 1$.

Table 2: Wake lengths for the flow past a circular cylinder at Carreau numbers $C_U = 10$ and $C_U = 20$ obtained for shear-thickening fluids with different values of the power index m.

	$m = 1.8$	$m = 1.6$	$m = 1.4$	$m = 1.2$	$m = 1$	$m = 0.8$	$m = 0.6$	$m = 0.4$	$m = 0.2$
$C_U = 10$	0	0	0.07309	0.135	0.2433	0.4387	0.8047	1.5566	3.1753
$C_U = 20$	0	0	0	0.08	0.2433	0.5768	1.2684	2.8044	6.066

the shear-thickening effects take place as m increases above 1, an adverse behavior occurs since larger shear rates outside the recirculation zone are expected to increase the viscosity and it causes more energy dissipation and shear stresses. Therefore, more fluid is entrained into the wake and the bubble length shrinks. These observations are in good agreement with the results presented in [39, 49] among others.

It is also clear from the obtained results that, for the same power index m, the shear-thinning fluids create a wider recirculation zone when the Carreau number increases from $C_U = 10$ to $C_U = 20$, while the shear-thickening flows have comparable wake bubble length for both selected Carreau numbers as it is confirmed by the precise bubble lengths reported in Table 2. Note that the expected zero recirculation lengths in Table 2 are explained by the fact that the apparition of a wake region for each Carreau number C_U and power index m depends on a critical value of the Reynolds number below of which there is no wake, see [49] for more detailed discussions. These observations are also in good agreement with the literature, see for example [52] for Newtonian fluids, [39, 49] for non-Newtonian fluids confirming that the proposed IVS method accurately captures the overall behavior of this class of generalized Newtonian fluid flows. To further demonstrate these effects we report in Table 3 the wake lengths obtained for shear-thinning fluids with different values of the power index m. For comparison, we also include results reported in [18] along with the relative difference between the two calculated wake lengths. It is clear that for all considered Carreau numbers and power indices, this difference does not exceed 2.75% which is good knowing that results reported in [18] used a very large domain to keep the boundary effects far away from the cylinder which is not the case in the proposed IVS method. The presented results, for this flow example, clearly demonstrate the performance of the IVS method and its ability to capture flow structures independently of the Carreau numbers and power indices which cover shear-thinning and shear thickening fluids. This also confirms that the proposed IVS method is very attractive since the computed flow solutions remain stable and accurate for generalized Newtonian fluid flow problems with natural boundary conditions.

4.4 Unsteady flow past two cylinders in tandem

Our final test example consists of an unsteady flow problem for a non-Newtonian fluid around an arrangement of two circular cylinders of diameter D one behind the other (in tandem). This class of flow problems past

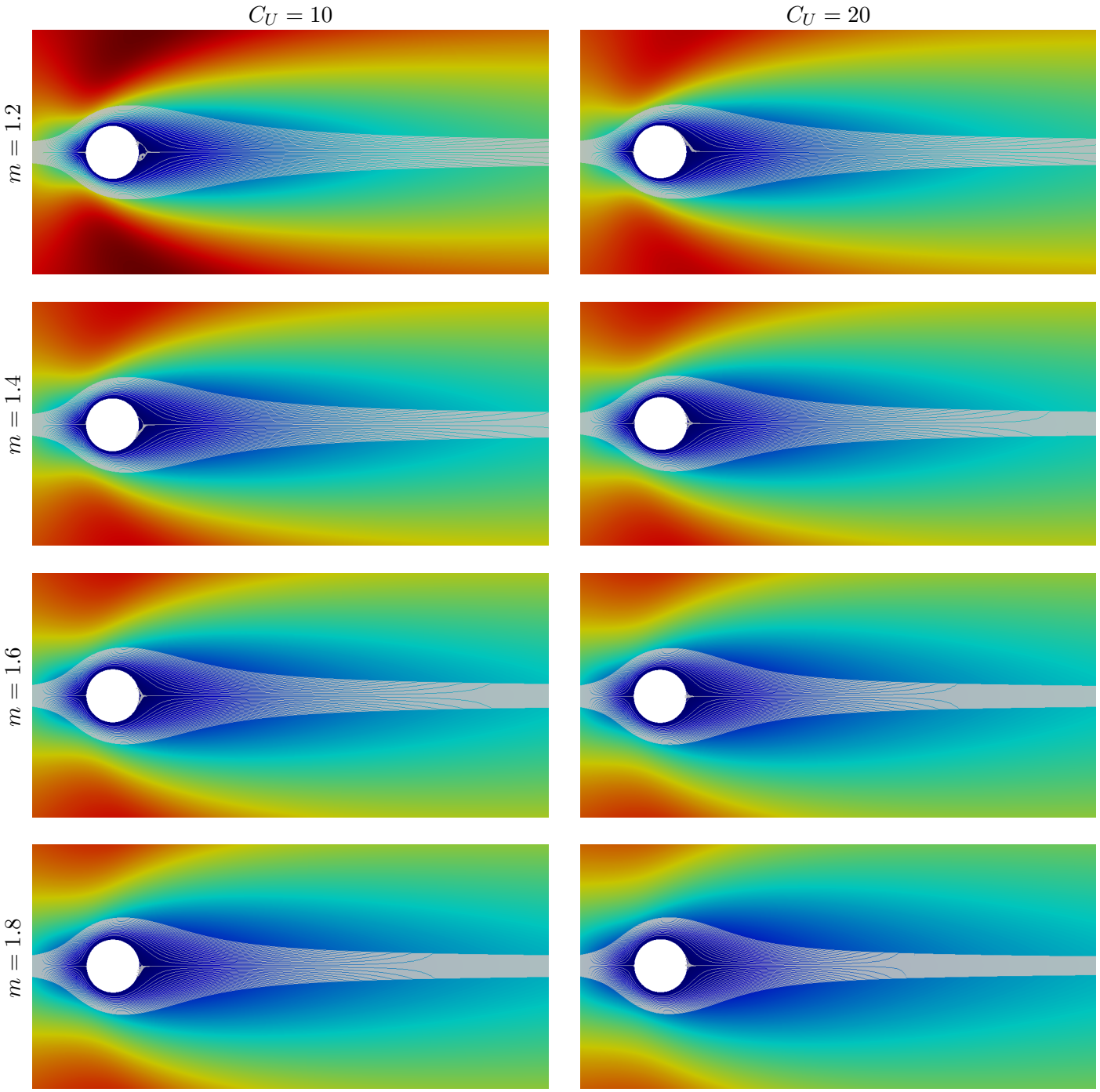

Figure 10: Streamlines and velocity magnitudes for the flow past a circular cylinder at Carreau numbers $C_U = 10$ (first column) and $C_U = 20$ (second column) obtained using the IVS method for shear-thickening fluids with $m = 1.2$ (first row), $m = 1.4$ (second row), $m = 1.6$ (third row) and $m = 1.8$ (fourth row).

arrangements of more than one cylinder covers many engineering applications such as wing trusts in aeronautics, radar masts, vibrations in hydranautics, vibrations of twin bundle conductor transmission lines in electrical engineering, vibrations in heat-exchangers in mechanical engineering among others. This flow configuration is also well studied and documented in the Newtonian case (see for example [60, 59]) however, it is less explored in the non-Newtonian case and only few published works can be found in the literature (see for example [51, 47, 46]). Here, we use the same computational domain as in the previous example, and a second cylinder of same diameter $D = 1$ is placed at a distance of $3D$ behind the first cylinder as shown in Figure 11. The flow

Table 3: Comparison of wake lengths for the flow past a circular cylinder at Carreau numbers $C_U = 10$ and $C_U = 20$ obtained for shear-thinning fluids with different values of the power index m.

	$C_U = 10$			$C_U = 20$		
m	Reference [18]	IVS	Error (in %)	Reference [18]	IVS	Error (in %)
1	0.2376	0.2433	2.40	0.2376	0.2433	2.40
0.9	0.3205	0.3293	2.75	0.3710	0.3804	2.53
0.8	0.4298	0.4387	2.07	0.5639	0.5768	2.29
0.7	0.5816	0.5942	2.17	0.8447	0.8576	1.53
0.6	0.7946	0.8047	1.27	1.2662	1.2684	0.17
0.5	1.1031	1.1118	0.79	1.9077	1.8872	1.07
0.4	1.5642	1.5566	0.49	2.8709	2.8044	2.32

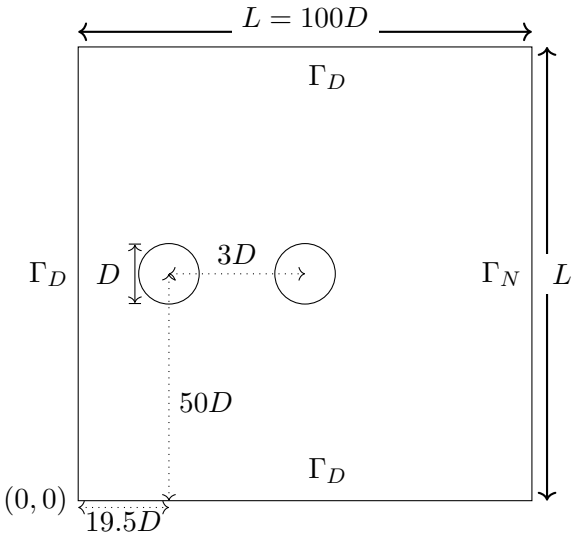

Figure 11: Configuration of the domain for the flow problem past two circular cylinders in tandem.

enters from the left with a velocity $u_\infty = 1$ and passes around the two cylinders on which the no-slip boundary conditions are imposed while outflow conditions are maintained on the domain outlet. On the top and bottom walls of the domain we use homogeneous Dirichlet boundary conditions. Note that the flow behavior in this configuration is affected by several parameters such as the Reynolds number Re, the gap between the two cylinders, the blockage ratio (D/L) and the non-Newtonian nature of the fluid which is assumed to follow the power-law (2) in our simulations. For this flow problem, the Reynolds number is defined by

$$Re = \frac{\rho u_\infty^{2-m} D^m}{C}.$$

In this unsteady flow problem, we are interested to study effects of the non-Newtonian nature of the fluid (shear-thinning or shear-thickening) represented by its power-index m on the flow patterns obtained using the proposed IVS method. Therefore, we fix the distance between the two cylinders to $3D$, the blockage ratio to 0.01 so the wall effects are negligible, and set $Re = 200$ which is high enough to enter the unsteady regime for the power-indexes $m \in \{0.4, 0.6, 1, 1.2, 1.4, 1.6, 1.8\}$ considered in our computations. Notice that for a detailed study on critical Reynolds numbers for this class of flow problems we refer to [51] and further references are therein.

In our simulations, the computational domain is discretized using an unstructured mesh consisting of 9204 mixed elements with 4695 pressure nodes and 18595 velocity nodes. The time step Δt is fixed to 0.1 and

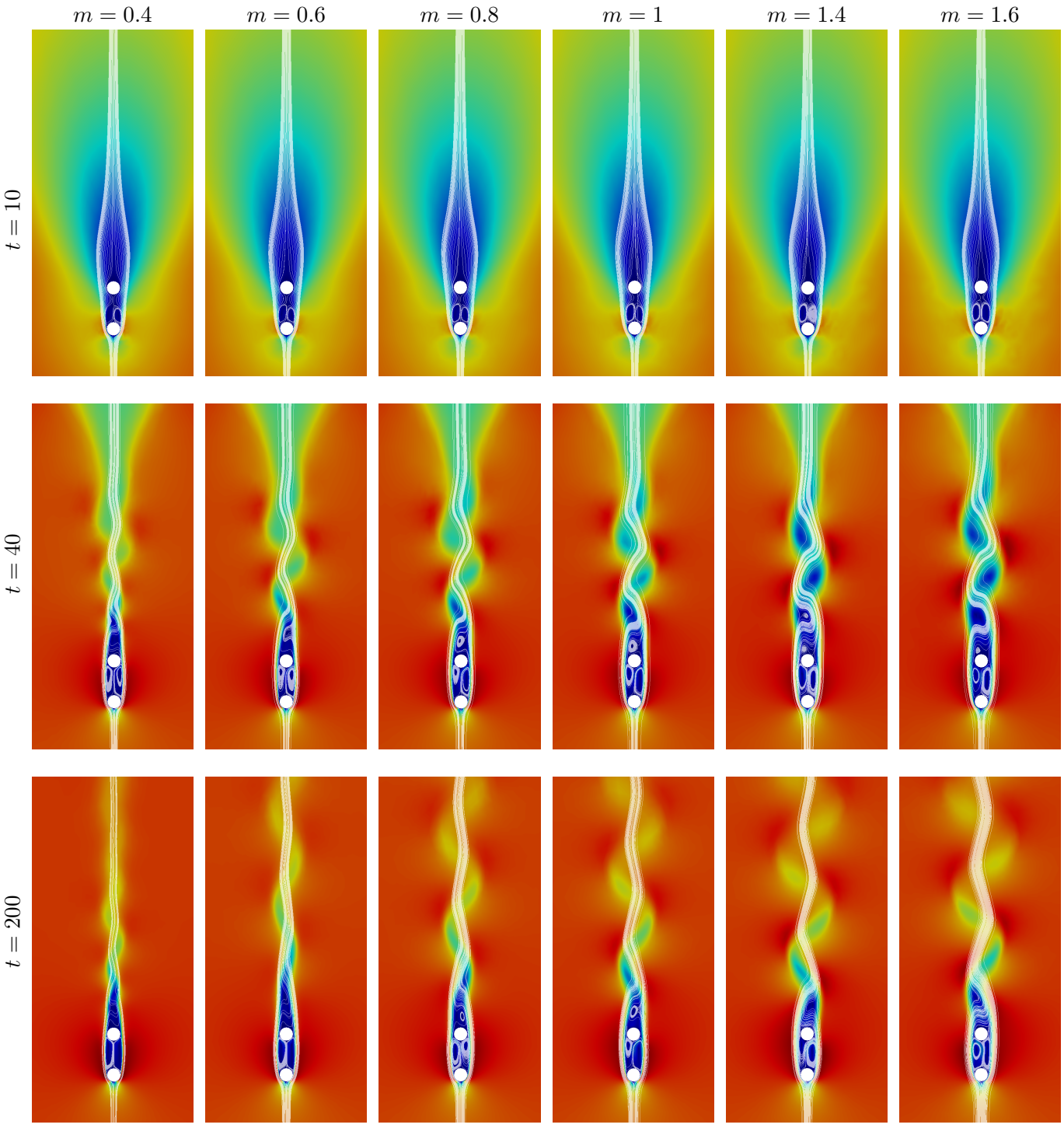

Figure 12: Streamlines and velocity magnitudes for the unsteady flow past two circular cylinders at $t = 10$ (first row), $t = 40$ (second row) and $t = 200$ (third row) obtained using the IVS method with $m = 0.4$ (first column), $m = 0.6$ (second column), $m = 0.8$ (third column), $m = 1$ (fourth column), $m = 1.4$ (fifth column) and $m = 1.6$ (sixth column).

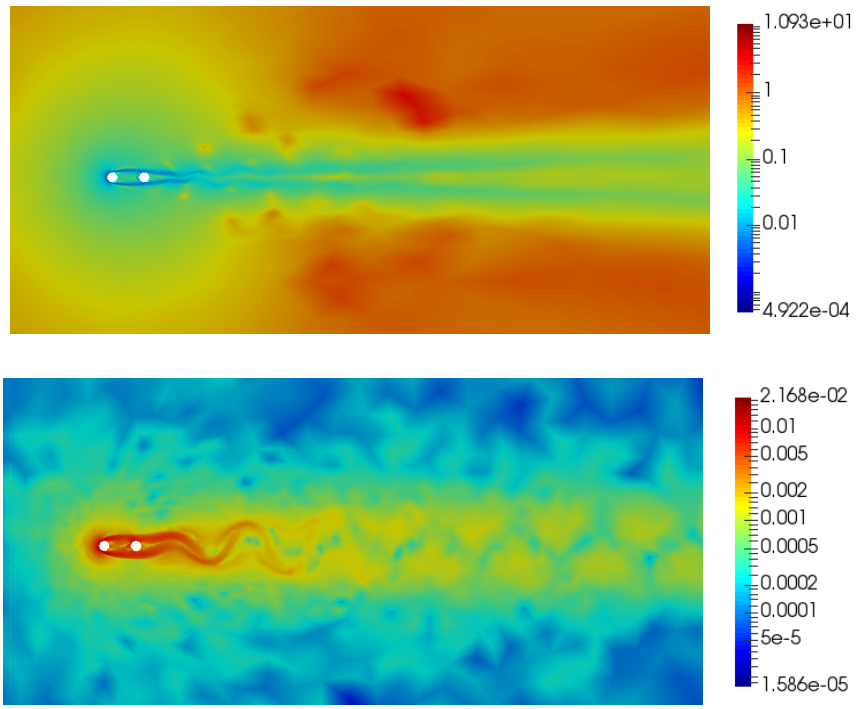

Figure 13: Viscosity distribution over the mainstream region for the unsteady flow past two circular cylinders at $t = 200$ using $m = 0.4$ (first row) and $m = 1.6$ (second row).

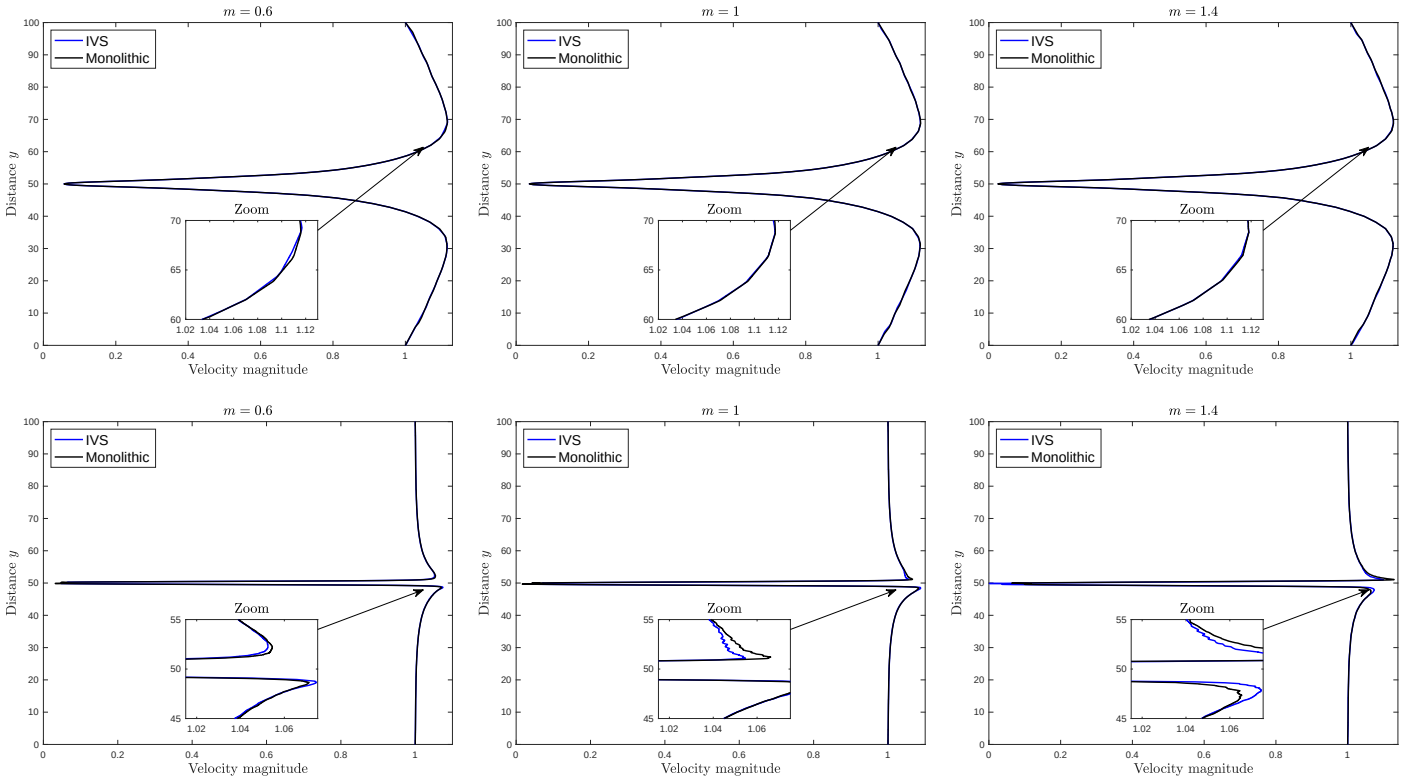

Figure 14: Velocity profiles along the vertical line located at $5D$ from the upstream cylinder center for the unsteady flow past two circular cylinders at $t = 10$ (first row) and $t = 200$ (second row).

numerical solutions obtained for velocity fields and streamlines are displayed at three different instants. Figure 12 depicts the streamlines and velocity magnitudes for $Re = 200$ and different values of the power-index m

Table 4: Maximum and minimum of the drag coefficients C_{D1} and C_{D2} on both cylinders for the unsteady flow past two circular cylinders obtained over the last 500 timesteps using the IVS and monolithic methods with different values of the power-index m.

		C_{D1}		C_{D2}	
		min	max	min	max
$m = 0.4$	IVS	0.7841	0.7996	-0.2039	-0.1921
	Monolithic	0.7769	0.7957	-0.2140	-0.2047
$m = 0.6$	IVS	0.8460	0.8582	-0.2043	-0.1904
	Monolithic	0.8255	0.8495	-0.2103	-0.1838
$m = 0.8$	IVS	0.9067	0.9227	-0.1935	-0.1662
	Monolithic	0.9065	0.9183	-0.1944	-0.1794
$m = 1$	IVS	0.9707	1.0048	-0.1729	-0.1523
	Monolithic	0.9830	0.9997	-0.1861	-0.1645
$m = 1.2$	IVS	1.0391	1.0582	-0.1646	-0.1431
	Monolithic	1.0310	1.0476	-0.1706	-0.1507
$m = 1.4$	IVS	1.0951	1.1103	-0.1643	-0.1371
	Monolithic	1.0895	1.1053	-0.1620	-0.1350
$m = 1.6$	IVS	1.1476	1.1545	-0.1541	-0.1176
	Monolithic	1.1515	1.1600	-0.1604	-0.1316
$m = 1.8$	IVS	1.2003	1.2209	-0.1605	-0.1168
	Monolithic	1.2070	1.2192	-0.1561	-0.1317

at $t = 10$, 40 and 200. It is clear that for all considered values of m, the flow develops an unsteady behavior as instabilities represented by trail oscillations and even vortex shedding for $m \geq 1$ take place behind the downstream cylinder in addition to a pair of non-symmetric rotating eddies behind the upstream cylinder. Note that in the Newtonian case, it is already known (see for instance [59]) that with a gape of $3D$ at low Reynolds numbers, no vortex shedding arises between the two cylinders, and the downstream cylinder is completely influenced by the wake of the first cylinder. This seems to be also valid for shear-thinning and shear thickening fluids as clearly shown in Figure 12. In fact, for all the flow regimes studied here, the detached free-shear layers from the upstream cylinder do not have enough space to converge behind it, so they reattach on the downstream cylinder whose wake exhibits a more complex behavior at $Re = 200$. Furthermore, effects of the power-index on the flow development especially behind the second cylinder can clearly be observed in this figure. For low values of the power-index $m < 1$, the trail oscillations are moderate with no vortex shedding yet. These oscillations become intensified as the power-index m goes further towards the Newtonian and shear-thickening cases where the beginning of vortex shedding becomes recognizable. This can be explained by the viscosity distribution for both shear-thinning and shear-thickening cases as displayed in Figure 13 for $m = 0.4$ and $m = 1.6$. In absence of wall effects (since these walls are positioned far away from the cylinders) it can be seen that for shear-thinning fluids, the mainstream is surrounded by wide areas of greater viscosity which enhances the viscous effects that in turn, tends to stabilize the flow due to the energy dissipation. On the other hand, the shear-thickening case shows only a concentrated region of important viscosity near the cylinders, while low viscosity is detected in most of the domain letting inertial forces to dominate and tend to push the flow towards instabilities.

Next, we turn our attention to the results obtained using the IVS method more closely by looking at the local physical quantities such as the drag coefficient and profiles of the vertical velocity which are of great interest in this class of flow simulations. For comparison, the same computations have been conducted by a monolithic method based on the mixed formulation of the original problem using the $\mathbb{P}_2$-$\mathbb{P}_1$ finite element approximation, see for example [26]. Note that the purpose here is not to evaluate the computational costs

of the two approaches as it is already known that a splitting method scores much better in CPU times when the problem under study is reasonably large. The purpose here is rather to assess the accuracy of the IVS method and its ability to overcome the associated splitting errors when applied to severe physical situations. For this reason, the monolithic approach being free from any splitting errors would be a significant reference for the evaluation. Table 4 summarizes the maximum and minimum values of the drag coefficients C_{D1} and C_{D2} on the two cylinders over the last 500 timesteps for both the IVS and monolithic methods, whereas Figure 14 presents the velocity profiles along the vertical line located at $5D$ from the upstream cylinder center at different instants. From Table 4 we can notice that the extremal values of the drag coefficients computed by both methods are close especially on the first cylinder with less than 3% of relative error, and around 11% error on the second cylinder when $m = 1.8$, bearing in mind that at $Re = 200$ and $m = 1.8$ the flow downstream the second cylinder undergoes more severe perturbations than the other cases, due to enhanced shear-thickening and vortex shedding as shown in Figure 12. Moreover, we notice from the same table that the drag is significantly more important on the upstream cylinder since it is facing the free stream. On the other hand, the second cylinder is submerged in a low pressure area behind the first cylinder while the pressure is greater on the back side. This difference in the adverse pressure results in a negative drag coefficient on the downstream cylinder in such a way that it feels being pushed against the flow direction which also explain the negative values appearing in Table 4 for C_{D2}. This qualitative behavior of the dag coefficient is in agreement with similar results published in the literature for the Newtonian case and it seems to be also valid for both shear-thinning and shear-thickening cases considered in this study. Under the selected flow conditions, the influence of the power-index is noticeable as the drag felt by both cylinders increases when m decreases for both shear-thinning and shear-thickening cases, with the increase being greater on the first cylinder. In addition, profiles of the vertical velocity in Figure 14 exhibit that the results obtained using the IVS method are in good agreement with those results obtained using the monolithic method and the both profiles, in all considered cases, are almost superposed except a small difference after the flow development near the middle axis that needed to be zoomed in to be visible. It should be noted that this small discrepancy is also observed in the Newtonian case, mainly due to the unsteady characteristics of the flow at $Re = 200$, and it is more intense as one goes towards shear-thickening cases for which the flow is more agitated as explained above. It is believed that this negligible discrepancy in the computed results can be considerably reduced using a finer mesh in the simulations. In conclusion, the comparison demonstrates overall that the IVS method is able to resolve, with satisfactory accuracy, the unsteady flow development even in agitated zones such as the downstream wake at a considerable Reynolds number.

5 Conclusions

In the present work we have presented an improved viscosity-splitting method for solving the generalized Newtonian fluids governed by generic models, which have sufficient flexibility to cover a wide variety of experimental viscosity versus shear-rate curves. The method consists of decoupling convective effects from the incompressibility constraint while keeping a diffusion term in the last step allowing to enforce consistent boundary conditions. The proposed method has the advantage of providing consistent pressure approximations without any boundary-layer drawbacks as those appeared in the standard projection or fractional-step methods. A pressure-correction strategy has also been introduced in this method to enhance its accuracy and a full algorithmic implementation of the method accounting for both Dirichlet and Neumann boundary conditions has been investigated. To assess the numerical performance of the proposed viscosity-splitting algorithm, we have presented computational results for an example with manufactured analytical solution and for the benchmark problems of lid-driven cavity flow and flow past a circular cylinder. Comparisons to the conventional viscosity-splitting algorithm have also been carried out in this study for the considered flow problems. The numerical results for the benchmark problems of lid-driven cavity flow and flow past a circular cylinder agree very well with other results from the literature. We have also examined the performance of the method for an unsteady flow around an arrangement of two cylinders in tandem and the comparisons with results obtained using the standard monolithic method reveal good general agreement. Future work will focus on the implementation of these techniques for thermal generalized Newtonian fluids. Furthermore, developing highly efficient solvers

for the associated linear systems in order to resolve issues related to the conditioning can further enhance the improved viscosity-splitting method. Extension of this method to the second-order accuracy using for example the second-order implicit backward differentiation formula is also part of our future work.

Data availability statement

The data that support the findings of this study are available from the corresponding author upon reasonable request.

Conflict of interest

The authors have no competing interests to declare that are relevant to the content of this paper.

References

[1] A. Aguirre, E. Castillo, M. Cruchaga, R. Codina, and J. Baiges. Stationary and time-dependent numerical approximation of the lid-driven cavity problem for power-law fluid flows at high Reynolds numbers using a stabilized finite element formulation of the vms type. *Journal of Non-Newtonian Fluid Mechanics*, 257:22–43, 2018.

[2] A. Amani, A. Naseri, C. D. Pérez-Segarra, and A. Oliva. A method for fluid-structure interaction problems with non-Newtonian fluid. In *Proceedings of the 6th European Conference on Computational Mechanics (Solids, Structures and Coupled Problems) and the 7th European Conference on Computational Fluid Dynamics, Glasgow, UK*, pages 101–110, 2018.

[3] H.-O. Bae. Regularity criterion for generalized Newtonian fluids in bounded domains. *Journal of Mathematical Analysis and Applications*, 421(1):489–500, 2015.

[4] H.-O. Bae and J. Wolf. Sufficient conditions for local regularity to the generalized Newtonian fluid with shear thinning viscosity. *Zeitschrift für angewandte Mathematik und Physik*, 68(1):7, Dec 2016.

[5] J. Blasco, R. Codina, and A. Huerta. A fractional-step method for the incompressible Navier–Stokes equations related to a predictor–multicorrector algorithm. *International Journal for Numerical Methods in Fluids*, 28(10):1391–1419, 1998.

[6] D. Boffi, F. Brezzi, and M. Fortin. *Mixed Finite Element Methods and Applications*, volume 44 of *Springer Series in Computational Mathematics*. Springer Berlin Heidelberg, Berlin, Heidelberg, 2013.

[7] J. H. Bramble and J. E. Pasciak. A preconditioning technique for indefinite systems resulting from mixed approximations of elliptic problems. *Mathematics of Computation*, 50(181):1–17, 1988.

[8] Z. Chai, B. Shi, Z. Guo, and F. Rong. Multiple-relaxation-time lattice Boltzmann model for generalized Newtonian fluid flows. *Journal of Non-Newtonian Fluid Mechanics*, 166(5-6):332–342, 2011.

[9] T.-F. Chen, C. L. Cox, H.-C. Lee, and K.-L. Tung. Least-squares finite element methods for generalized Newtonian and viscoelastic flows. *Applied numerical mathematics*, 60(10):1024–1040, 2010.

[10] T.-F. Chen, H. Lee, and C.-C. Liu. Numerical approximation of the oldroyd-b model by the weighted least-squares/discontinuous Galerkin method. *Numerical Methods for Partial Differential Equations*, 29(2):531–548, 2013.

[11] A. J. Chorin. Numerical solution of the Navier-Stokes equations. *Mathematics of computation*, 22(104):745–762, 1968.

[12] P. Coelho and F. Pinho. Vortex shedding in cylinder flow of shear-thinning fluids: I. identification and demarcation of flow regimes. *Journal of non-Newtonian fluid mechanics*, 110(2-3):143–176, 2003.

[13] P. Coelho and F. Pinho. Vortex shedding in cylinder flow of shear-thinning fluids: II. flow characteristics. *Journal of non-Newtonian fluid mechanics*, 110(2-3):177–193, 2003.

[14] P. Coelho and F. Pinho. Vortex shedding in cylinder flow of shear-thinning fluids. III: Pressure measurements. *Journal of non-Newtonian fluid mechanics*, 121(1):55–68, 2004.

[15] O. M. Coronado, D. Arora, M. Behr, and M. Pasquali. Four-field Galerkin/least-squares formulation for viscoelastic fluids. *Journal of non-Newtonian fluid mechanics*, 140(1-3):132–144, 2006.

[16] W. Couzy. Spectral element discretization of the unsteady Navier-Stokes equations and its iterative solution on parallel computers. Technical report, EPFL, 1995.

[17] J. Deteix and D. Yakoubi. Improving the pressure accuracy in a projection scheme for incompressible fluids with variable viscosity. *Applied Mathematics Letters*, 79:111–117, 2018.

[18] J. Deteix and D. Yakoubi. Shear rate projection schemes for non-Newtonian fluids. *Computer Methods in Applied Mechanics and Engineering*, 354:620–636, 2019.

[19] L. Diening, M. Růžička, and J. Wolf. Existence of weak solutions for unsteady motions of generalized Newtonian fluids. *Ann. Sc. Norm. Super. Pisa Cl. Sci. (5)*, 9(1):1–46, 2010.

[20] Y. I. Dimitrienko and S. Li. Numerical simulation of MHD natural convection heat transfer in a square cavity filled with Carreau fluids under magnetic fields in different directions. *Computational and Applied Mathematics*, 39(4):252, 2020.

[21] P. Dreyfuss and N. Hungerbühler. Results on a Navier-Stokes system with applications to electrorheological fluid flow. *Int. J. Pure Appl. Math.*, 14(2):241–271, 2004.

[22] X. Escriva, E. Leriche, and T. N. Phillips. Preconditioned uzawa algorithm for the velocity-pressure-stress formulation of viscoelastic flow problems. *Journal of scientific computing*, 17:201–210, 2002.

[23] N. Fiétier and M. O. Deville. Simulations of time-dependent flows of viscoelastic fluids with spectral element methods. *Journal of scientific computing*, 17:649–657, 2002.

[24] W. Gao and R. Liu. A hybrid finite volume/finite element method for incompressible generalized Newtonian fluid flows on unstructured triangular meshes. *Acta Mechanica Sinica*, 25(6):747, 2009.

[25] U. Ghia, K. N. Ghia, and C. Shin. High-re solutions for incompressible flow using the Navier-Stokes equations and a multigrid method. *Journal of computational physics*, 48(3):387–411, 1982.

[26] V. Girault and P.-A. Raviart. *Finite Element Methods for the Navier-Stokes Equations*, volume 5 of *Springer Series in Computational Mathematics*. Springer-Verlag, Berlin, 1986.

[27] R. Glowinski, T.-W. Pan, and J. Periaux. A fictitious domain method for external incompressible viscous flow modeled by Navier-Stokes equations. *Computer Methods in Applied Mechanics and Engineering*, 112(1-4):133–148, 1994.

[28] K. Goda. A multistep technique with implicit difference schemes for calculating two-or three-dimensional cavity flows. *Journal of computational physics*, 30(1):76–95, 1979.

[29] G. H. Golub and C. F. Van Loan. Matrix computations, secondedition, 1989.

[30] A. González, R. Cabrales, and E. Castillo. Numerical study of the use of residual-and non-residual-based stabilized VMS formulations for incompressible power-law fluids. *Computer Methods in Applied Mechanics and Engineering*, 400:115586, 2022.

[31] A. González, O. Ruz, and E. Castillo. Numerical study of the fluid dynamics and heat transfer for shear-thinning nanofluids in a micro pin-fin heat sink. *Case Studies in Thermal Engineering*, 28:101635, 2021.

[32] P. M. Gresho. On the theory of semi-implicit projection methods for viscous incompressible flow and its implementation via a finite element method that also introduces a nearly consistent mass matrix. part 1: Theory. *International Journal for Numerical Methods in Fluids*, 11(5):587–620, 1990.

[33] J. Guermond and J. Shen. On the error estimates for the rotational pressure-correction projection methods. *Mathematics of Computation*, 73(248):1719–1737, 2004.

[34] J.-L. Guermond, P. Minev, and J. Shen. An overview of projection methods for incompressible flows. *Computer methods in applied mechanics and engineering*, 195(44-47):6011–6045, 2006.

[35] A. Ibarz and G. V. Barbosa-Cánovas. *Unit operations in food engineering*. CRC press, 2002.

[36] G. D. Ilio, D. Chiappini, and G. Bella. A comparison of numerical methods for non-Newtonian fluid flows in a sudden expansion. *International Journal of Modern Physics C*, 27(12):1650139, 2016.

[37] F. Irgens. *Rheology and non-Newtonian fluids*, volume 1. Springer, 2014.

[38] M. Jabbari, J. McDonough, E. Mitsoulis, and J. H. Hattel. Application of a projection method for simulating flow of a shear-thinning fluid. *Fluids*, 4(3):124, 2019.

[39] I. Lashgari, J. O. Pralits, F. Giannetti, and L. Brandt. First instability of the flow of shear-thinning and shear-thickening fluids past a circular cylinder. *Journal of fluid mechanics*, 701:201–227, 2012.

[40] H.-C. Lee and H. Lee. Numerical simulations of viscoelastic fluid flows past a transverse slot using least-squares finite element methods. *Journal of Scientific Computing*, 79(1):369–388, 2019.

[41] S. Li and Y. I. Dimitrienko. Least squares finite element simulation of local transfer for a generalized Newtonian fluid in 2D periodic porous media. *Journal of Non-Newtonian Fluid Mechanics*, 316:105032, 2023.

[42] J. Liu. Open and traction boundary conditions for the incompressible Navier–Stokes equations. *Journal of Computational Physics*, 228(19):7250–7267, 2009.

[43] Y. Lung-an. Viscosity-splitting scheme for the Navier-Stokes equations. *Numerical Methods for Partial Differential Equations*, 7(4):317–338, 1991.

[44] Y. Maday, A. T. Patera, and E. M. Rønquist. An operator-integration-factor splitting method for time-dependent problems: application to incompressible fluid flow. *Journal of Scientific Computing*, 5:263–292, 1990.

[45] R. Natarajan. A numerical method for incompressible viscous flow simulation. *Journal of Computational Physics*, 100(2):384–395, 1992.

[46] A. Nejat, V. Abdollahi, and K. Vahidkhah. Lattice boltzmann simulation of non-Newtonian flows past confined cylinders. *Journal of Non-Newtonian Fluid Mechanics*, 166(12-13):689–697, 2011.

[47] A. Nejat, E. Mirzakhalili, A. Aliakbari, M. S. F. Niasar, and K. Vahidkhah. Non-Newtonian power-law fluid flow and heat transfer computation across a pair of confined elliptical cylinders in the line array. *Journal of Non-Newtonian Fluid Mechanics*, 171:67–82, 2012.

[48] D. R. Pacheco, R. Schussnig, and T.-P. Fries. An efficient split-step framework for non-Newtonian incompressible flow problems with consistent pressure boundary conditions. *Computer Methods in Applied Mechanics and Engineering*, 382:113888, 2021.

[49] A. Pantokratoras. Steady flow of a non-Newtonian Carreau fluid across an unconfined circular cylinder. *Meccanica*, 51(4):1007–1016, Apr. 2016.

[50] L. Plasman, J. Deteix, and D. Yakoubi. A projection scheme for Navier-Stokes with variable viscosity and natural boundary condition. *International Journal for Numerical Methods in Fluids*, 92(12):1845–1865, 2020.

[51] O. Ruz, E. Castillo, M. Cruchaga, and A. Aguirre. Numerical study of the effect of blockage ratio on the flow past one and two cylinders in tandem for different power-law fluids. *Applied Mathematical Modelling*, 89:1640–1662, 2021.

[52] S. Sen, S. Mittal, and G. Biswas. Steady separated flow past a circular cylinder at low Reynolds numbers. *Journal of Fluid Mechanics*, 620:89–119, 2009.

[53] Z. Tan and J. Zhou. Partial regularity of a certain class of non-Newtonian fluids. *Journal of Mathematical Analysis and Applications*, 455(2):1529 – 1558, 2017.

[54] R. Temam. Sur l'approximation de la solution des équations de Navier-Stokes par la méthode des pas fractionnaires (ii). *Archive for rational mechanics and analysis*, 33:377–385, 1969.

[55] R. Temam. Remark on the pressure boundary condition for the projection method. *Theoretical and Computational Fluid Dynamics*, 3(3):181–184, 1991.

[56] L. J. Timmermans, P. D. Minev, and F. N. Van De Vosse. An approximate projection scheme for incompressible flow using spectral elements. *International journal for numerical methods in fluids*, 22(7):673–688, 1996.

[57] J. Van Kan. A second-order accurate pressure-correction scheme for viscous incompressible flow. *SIAM journal on scientific and statistical computing*, 7(3):870–891, 1986.

[58] D. Yakoubi. Enhancing the viscosity-splitting method to solve the time-dependent Navier–Stokes equations. *Communications in Nonlinear Science and Numerical Simulation*, 123:107264, 2023.

[59] M. Zdravkovich. The effects of interference between circular cylinders in cross flow. *Journal of fluids and structures*, 1(2):239–261, 1987.

[60] M. Zdravkovich and D. Pridden. Interference between two circular cylinders; series of unexpected discontinuities. *Journal of wind engineering and industrial aerodynamics*, 2(3):255–270, 1977.